UNIVERSITÀ DEGLI STUDI DI PADOVA

Dipartimento di Fisica e Astronomia "Galileo Galilei"

Corso di Laurea Magistrale in Fisica

Tesi di Laurea

Simulation and calibration of detectors for the ^{4}n and ^{7}H experiment at SAMURAI, RIKEN

Relatore

Prof. Marco Mazzocco

Correlatori

Prof. Julien Gibelin

Prof. F. Miguel Marqués

Prof. Adrien Matta

Laureando

Elidiano Tronchin

Anno Accademico 2018/2019

ACKNOWLEDGMENTS

This thesis was financed by the french Centre National de la Recherche Scientifique (CNRS) through the internship at the Particle Physics Laboratory (LPC) in Caen during the Erasmus+ mobility term.

Author is grateful to Prof. J. Gibelin for the valuable advice on how to deal with unexpected analysis problems, to Prof. F. M. Marqués for the fascinating theoretical explanations, Prof. A. Matta for his assistance with NPTool and his empathy, and to all the administration and technicians for the help provided during the stay at LPC.

Also thanks to Prof. M. Mazzocco for his help and suggestions during the thesis writing and his availability.

Abstract

In the light of the apparent binding effect of neutrons in the extremely neutron-rich light nuclei (^{5,6}H and ^{6,7,8}He) and of the surprising long life-time of ^{8}He ($\tau \simeq 1.19 \times 10^{2}$ ms), the SAMURAI 34 experiment aimed at definitively proving the existence of both ^{7}H and ^{4}n by making use of the same reaction ^{8}He(p, 2p)^{7}H through the knock-out technique.

We describe the experimental setup used, focusing on DALI, 36 NaI crystals, and MINOS, a vertex tracker coupled to a thick liquid-hydrogen target. The beginning of the data analysis for the two detectors is exposed, and new simulation tools are developed in order to facilitate the calibration procedure.

The kinematics of the calibration reaction is given, evaluating its relativistic nature.

The problems encountered in the MINOS calibration are described and the possible causes explained. Different procedures were adopted finding conflicting results regarding the quality of the obtained results.

Finally, the next steps for the data analysis are given, considering the perspectives on the possibility of obtaining results after the verified issues.

Keywords— many-neutron system, tetraneutron, hydrogen, DALI, MINOS, active target, TPC, simulation, NPTool, elastic scattering

Sommario

Dopo numerosi tentativi i cui risultati soffrirono sempre di scarsa risoluzione e statistica, l'esperimento SAMURAI 34 si propone di provare definitivamente l'esistenza di ^{7}H e ^{4}n. Questo è possibile attraverso la medesima reazione di knock-out ^{8}He(p, 2p)^{7}H e lo studio dei prodotti di reazione tramite un'orchestra di rivelatori.

Particolare attenzione è data nel lavoro di tesi a due rivelatori: DALI, formato da 36 cristalli di NaI, e MINOS, composto dal bersaglio di idrogeno liquido circondato dalla camera di tracciamento. L'inizio della procedura di calibrazione e le simulazioni implementate per lo studio e l'analisi dell'esperimento sono descritti.

La cinematica dell'urto elastico tra due protoni è valutata, considerando un regime relativistico in vista della calibrazione tramite tale reazione.

Sono poi descritti i problemi riscontrati nella calibrazione di MINOS, offrendo nuove modalità di analisi per la valutazione della bontà dei risultati ottenuti.

Sono quindi stabiliti i necessari accorgimenti per proseguire la calibrazione e sono valutati i limiti che per ora i problemi sorti hanno posto ai risultati sperimentali.

Parole chiave— sistemi a molti neutroni, tetraneutrone, idrogeno, DALI, MINOS, active target, TPC, simulazione, NPTool, urto elastico

CONTENTS

LIST OF FIGURES

LIST OF TABLES

1 INTRODUCTION

1.1 IMPORTANCE OF STUDIES ABOUT NEUTRON DRIP LINE

Very light nuclei have longly played a fundamental role in testing nuclear models and the underlying nucleon-nucleon (N-N) interaction. Whilst much effort has been devoted in attempting to model stable systems, yet a number of ambiguities remains. For this, the study of systems exhibiting very asymmetric N/Z ratios may provide new perspectives on the N-N interaction and few-body forces. Several reaction methods are used in these studies at the drip lines, including knock-out reactions described in Section 1.3. Moreover the extreme fraction of neutron-to-proton ratio N/Z, makes these systems interesting also for the comparison with neutrons stars.

1.2 LOOKING FOR ^{7}H AND ^{4}n

There has been debate since the beginning of 1960s about the possible existence of neutral nuclei [SV63]. Based on the present knowledge of the nuclear interaction, a multi-neutron system should not exist, but many proposals have been put forward in favor of it.

Indeed for several neutron-rich nuclei an interesting common behaviour was observed. As reported in [MM03], usually the binding energy decreases monotonically as more and more neutrons are added to a nuclear system, but not for hydrogen and helium. On the contrary it seems that 4 neutrons give a binding effect for helium, indeed for example $\alpha + 4n$ and $^{5}\mathrm{He} + 4n$ lead respectively to the stable against particle emission ^{8}He ($\tau \simeq 1.19 \times 10^{2}$ ms) and the very slightly unbound ^{9}He nuclei [For+06].

In the same way, as shown in Fig.1, the sequence of H at several A values is modulated by the $\pm\delta$ pairing term. This modulation occurs also in the isotone line $N = 4$ with a $+\delta$ contribution in the correspondence of the neutral nucleus, namely the tetraneutron ^{4}n.

The work presented here is part of an experiment (SAMURAI 34 -S34-) whose aim was to definitively prove the existence of both ^{7}H and ^{4}n, and in case of a positive result, to measure their detailed spectroscopy.

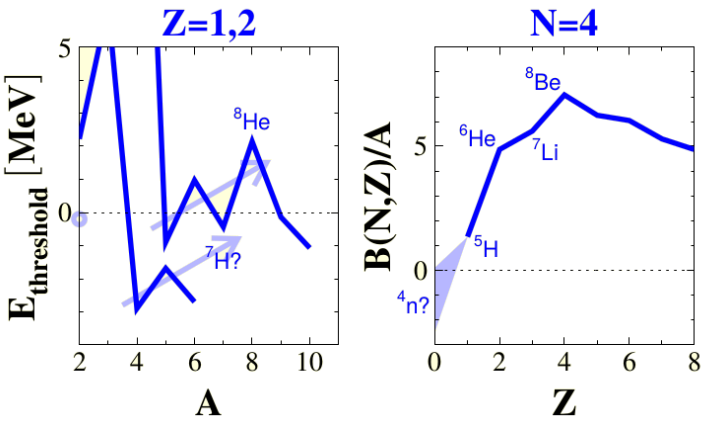

Figure 1: At left: binding energy oscillation for the isotope lines $Z = 1, 2$ with respect to the first particle threshold; at right: binding energy of the isotone line $N = 4$. Courtesy of F. M. Marqués (LPC).

Indeed if the analysis of ^{7}H confirms the binding contribution of the 4n, we can expect also a stability of the latter as a bound system. In fact, although ^{4,5}H are not stable, this is not in contradiction with a possible ^{4}n stability. The hydrogen isotopes have a positive binding energy of about $6\,MeV$, but they are unbound only because the triton is bound by $7.7\,MeV$. In the same way ^{7}H should undergo the decay into $t + 4n$ and its width may be very narrow. This was confirmed in the first evidence for the existence of this nucleus, observed in 2003 [Kor+03] using the same reaction of this experiment, but at a beam energy about one third ($E_{beam} \simeq 60\,MeV$) of ours. The resonance of ^{7}H is expected to be about $0.6(3)\,MeV$ –or less– above the $^{3}H + 4n$ threshold as found in 2007 [Cn+07; Cn+08].

In the case of ^{4}n there are no bound subsystems, and therefore any positive value of binding energy, even very small, would lead to a bound tetraneutron. Furthermore we could state that this nuclear configuration would be really stable, if it were not for the weak force acting as beta decay of the neutrons. Despite hopes, all results from theoretical studies exclude any bound tetraneutron [Tim03; BZ03; Pie03], but they do not preclude a possible resonance around $2\,MeV$ above the threshold [Pie03], although it should contemplate a very strong nuclear four-body force currently unknown [LC05].

All this makes the study of these two states very interesting and crucial for a deeper knowledge of N-N interactions.

1.3 EXPERIMENT

In order to produce the ^{7}H, the knock-out technique was used in this experiment. It is a direct reaction, i.e. a direct transition of the original nuclei of the beam into a final state without the formation of an intermediate compound nucleus. The final states of the reaction are identified observing the outgoing

products. In particular, the knock-out technique refers to the ejection of one component –of the projectile– which interacts with the target nucleus.

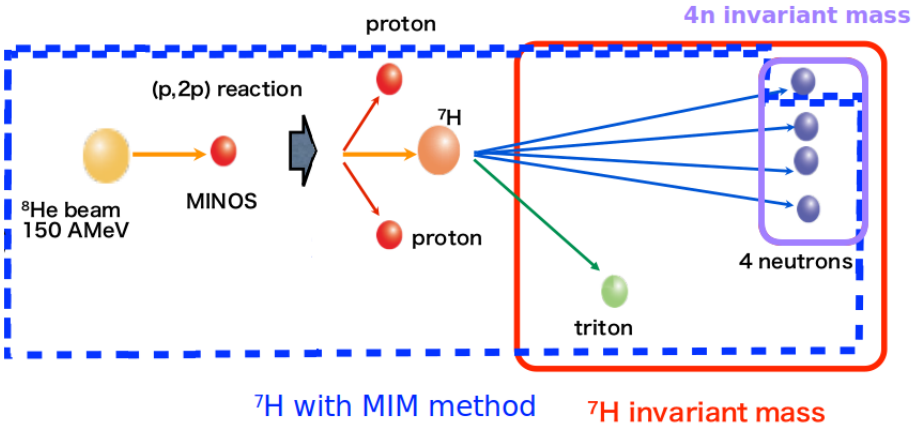

Figure 2: Reaction ^{8}He(p, 2p)^{7}H and the decay $^{7}H \rightarrow t + 4n$. In red solid lines the elements for the ^{7}H invariant mass, in blue dotted lines the elements for the ^{7}H with MIM method (cfr. Sec. 1.3.1), in violet the elements for the 4n invariant mass.

To study the ^{7}H the reaction chosen here was ^{8}He(p, 2p)^{7}H[1] where a beam of ^{8}He interact with a proton of the target. Then one proton of the ^{8}He is removed producing the ^{7}H. The reaction itself is identified with the detection of two protons in the detector arrays surrounding the target.

The signature of the ^{7}H production, being unbound, is the detection of a triton (the nucleus of a tritium) in the fragment detector.

Moreover, as ^{7}H will decay into a triton and 4n, it will be possible to study at the same time the existence of a possible tetra-neutron system.

As reported in the proposal of this experiment, the cross section of ^{8}He(p, 2p)^{7}H reaction was estimated to be about 1 mb by the previous experiment with the incident energy of 200 *MeV/nucleon* [Kob+00a]. This small cross section implied to increase the beam intensity as well as to increase the thickness of the target. Hence, in order to reconstruct the reaction vertex with a reasonable position resolution, an active target was used.

Finally, two techniques are used to gain information on the nuclei of interest: the invariant and the missing mass methods that will be described in the following sections.

1 The reaction is in inverse kinematics and for conventions, the correct way to express the reaction would have been p(^{8}He, 2p)^{7}H, but for a mere and arbitrary aesthetics consideration we will use the form ^{8}He(p, 2p)^{7}H.

1.3.1 Missing mass and invariant mass methods

The *invariant mass method* consists in measuring all information (energy and momentum) of the outgoing particles from the system which we are interested. Hence here the invariant mass of ^{7}H is reconstructed from the energies and the momenta of the triton and of the 4 neutrons.

In addition, since we have access to the complete 7-body kinematics of the final state (2p+t+4n), the invariant mass of ^{7}H can also be reconstructed from the momenta of only 3 of the neutrons, thanks to the *missing mass method*.

The combination of these two methods is called Missing+Invariant Mass (MIM) method, and it can be helpful for low statistics experiments and low energy particles.

Missing mass method

The four-momentum $\left(E_{miss}, \vec{P}_{miss}\right)$ of the undetected neutron can be reconstructed since all of the other momenta of the particles are measured.

The missing mass method is based on the conservation laws of the energy and momentum for which the missing mass can be reconstructed through the formula:

$$M_{miss}^2 = \left(\sum_{reagents} E_i - \sum_{products} E_j \right)^2 - \left(\sum_{reagents} \vec{P}_i - \sum_{products} \vec{P}_j \right)^2 ,$$

where the sums on the momenta and energies of the products do not obviously include that of the desired (undetected) particle.

Since the neutron mass is known, and to obtain the invariant mass of ^{7}H we are interested to the unknown momentum $\left(E_{miss}, \vec{P}_{miss}\right)$ of one neutron, obtainable through direct conservation law:

$$E_{miss} = \sum_{reagents} E_i - \sum_{products} E_j,$$

$$\vec{P}_{miss} = \sum_{reagents} \vec{P}_i - \sum_{products} \vec{P}_j.$$

Invariant mass method

The invariant mass of ^{7}H,

$$M = \sqrt{\left(\sum_{i=daughters} E_i \right)^2 - \left(\sum_{i=daughters} \vec{P}_i \right)^2} ,$$

is directly reconstructed from the measured momenta $\vec{P}_i$ of the decay products. The decay energy E_{decay} is calculated as

$$E_{decay} = M - \sum_i m_i,$$

where m_i are the masses of the decay products.

Advantages of the MIM method

In case of need, due to a missing neutron, the invariant mass can be reconstructed as

$$M = \sqrt{\left(\sum_i E_i + E_{miss}\right)^2 - \left(\sum_i \vec{P}_i + \vec{P}_{miss}\right)^2}.$$

This MIM method can be crucial if the ground state of ^{7}H is extremely close to the threshold, since at such low energies the 3n efficiency can be about 10 times higher than the 4n one. For decay energies lower than $1\,MeV$ the MIM method is more and more helpful. The detection efficiency of 3n and 4n are estimated to be 8% and 0.7% , respectively, for $E_{decay} = 1\,MeV$ following phase-space decay. This means, including the protons detection, the total detection efficiency of the MIM method is 5 times larger than the simple invariant mass one.

Obviously a drawback of this method could be the worse energy resolution of the calculated invariant mass. Indeed, at very low decay energies, the energy resolution can become twice as large.[2]

1.4 SUBJECT OF THIS WORK

In order to analyse the overall amount of data collected during the experiment, my main contribution was to start the calibration of the experimental setup, specifically for two detectors: DALI and MINOS. I contributed to the analysis and also on simulation tools to handle the experimental data and the results of the simulations.

DALI is a 36 NaI crystals array (cfr. Sec. 2.3), and it was used to detect the protons knocked-out from the reaction measuring their energy. MINOS, a time projection chamber (cfr. Sec. 2.2), was employed as a tracking detector for the two protons. Combining their information it will be possible to extract their energy at the reaction vertex, and then take advantage of the MIM method of Sec. 1.3.1.

2 Cfr. S34 proposal.

2 EXPERIMENTAL SETUP

2.1 GENERAL DESCRIPTION OF TOTAL APPARATUS

The S34 experiment was performed at RIKEN in 2017 and it was based on the SAMURAI setup illustrated on Fig. 3. This consists principally of a large magnetic dipole, namely **SAMURAI**, coupled to charged fragment tracking detectors, the Focal Drift Chambers FD1 and FD2, and to an array of plastic detectors, the **HODOSCOPE** [RIK08]. In order to measure neutrons the **NEBULA** detector array was located downstream the beam. Details concerning the whole SAMURAI setup can be found in the comprehensive publication [Kob+13].

More specifically this experiment other multi-detectors were added: an additional neutron detector **NeuLAND**, and the **MINOS** active target coupled to a **NaI crystals** array from DALI2[1]. MINOS and DALI[2] are in yellow and green on Fig. 3, respectively.

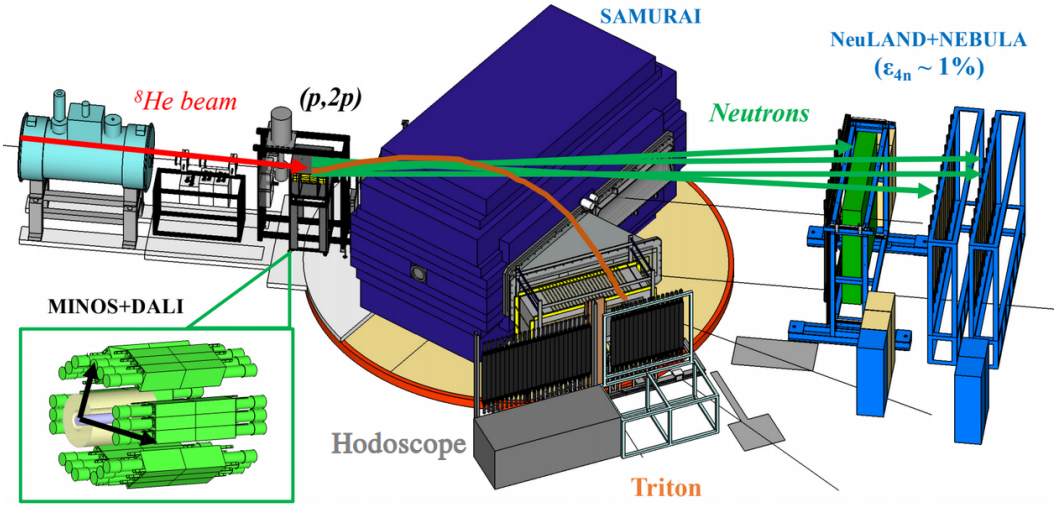

Figure 3: Experimental setup for ^{8}He(p,2p)^{7}H reaction studied in S34 experiment at RIKEN. Courtesy of Z.H. Yang (RIKEN Nishina Center).

The **cylindrical configuration** of detectors surrounding the target was chosen after detailed kinematical simulation of the reaction of interest, taking into con-

1 Usually for gamma detection but here for charged particles.
2 This is the name we will use to refers to the NaI crystals system.

sideration the reaction Q value, the Fermi momentum of the knock-out proton and the target geometry. This permits the detection of the protons emitted from the ^{8}He(p,2p)^{7}H reaction covering the polar angle $\theta_{lab} = [20° ; 55°]$.

After briefly describing the radioactive ion beam used, we present the arrays used in this experiment, focusing our attention on the two detectors which were the main subject of this thesis work: **DALI** and **MINOS**.

2.1.1 ^{8}He Beam production

The **^{8}He beam** for the S34 experiment was produced by fragmentation [Kub03]. This in-flight method, also simply called "fragmentation", is well adapted to the study of nuclei with short lifetime. This method exploits the kinematic properties of the nuclear reactions used in the RIB production and saving the high linear momentum. In fact it is necessary to have a narrow opening of the kinematic cones in the target reactions to permit the tagging and the analysis of the products by the fragment analyser.

At first, in the primary reaction, a stable heavy-ion beam impinges onto a light production target. This ensures the fragments of the beam are retained with an high momentum. Several unstable ions produced by this technique are in-flight separated in A and Z by means of electric and magnetic fields. The fragment separator, used at the Radioactive Ions Beam Factory (RIBF), is called BigRIPS [Kub03]. In our case the primary beam was ^{18}O on a ^{9}Be target. The production rate was about one ^{8}He nucleus every million ^{18}O nuclei.

The secondary beam produced and selected has a velocity similar to that of the stable primary beam used –nearly 60% of the speed of light– which enables their transport to the experimental area. The beam rate was about 9×10^{4} pps at 156 MeV/A for ^{8}He and 11×10^{4} pps at 176.78 MeV for the calibration runs with the proton beam.

A drawback of this method is the usually poor ion optical quality of the beam. Hence, the trajectory of the beam is reconstructed event by event by using two position sensitive drift chambers, called BDC1 and BDC2 (Beam Drift Chambers). Detailed information about the drift chambers for the particle detection is available in [BRR08], and a technical description of BDCs is presented in Ref. [RIK06].

In order to identify the incoming nuclei and to provide a time reference for the experiment, two thin plastic detectors, called Secondary Beam Triggers (SBTs), were placed along the beam line just before the BDCs.

The particle distribution was estimated to be about 8 mm (FWHM) in the x and y axis in the target. This value and the angular spread will be ascertained in the BDCs analysis.

2.1.2 Detector arrays

We briefly describe here all the detectors employed in this experiment. A detailed description of MINOS and DALI, used in this work, will be given in Sec. 2.2 and 2.3.

SAMURAI. The superconductor magnet SAMURAI (Superconducting Analyzer for MUlti-particles from RAdio Isotopes beams) allows the separation of the charged fragments emitted during the reaction and to reconstruct their kinematic properties. SAMURAI is able to create a relatively homogeneous vertical magnetic field up to 3.1 T between the poles for a current of 563 A. Such a field corresponds to a bending power (field integral) up to 7 T m and can separate charged fragments (in mass and charge) by nearly 5σ for an energy of 250 MeV/A and a $A/Z \simeq 3$ ratio. [Sat+13]

HODOSCOPE. This charged particle detector is made up of 24 plastic scintillators of $100 \times 1200 \times 10\,mm^3$. It records the energy loss and the time signal of the fragments outgoing from the reaction. It also allows, by combining this information with the rigidity deduced from SAMURAI, to identify the reaction products.

NEBULA. It is a neutron detector made of plastic scintillators and positioned in the beam direction. It is made of 120 plastic scintillator bars organized in two walls separated by 85 cm. Each wall is made of two layers of 30 bars of dimensions $120 \times 1800 \times 120\,mm^3$ placed vertically, each time preceeded by a charged particle veto detector. These vetos are plastic scintillators thinner enough to have a negligible efficiency to neutron detection but sufficient to allow the detection of charged particles. A photomultiplier is placed at the edge of each bar allowing the measurement of the interaction of the neutron.

Neutron detection is indirect, being induced by the signal of the recoil nuclei coming from a nuclear reaction. This implies that the energy deposited in the detector is not proportional to that of the incident neutron. A measurement of target-NEBULA ToF, based on the SBTs time trigger (cfr. Sec. 2.1.1), is used in order to determine the energy of the neutron.

NeuLAND. This second neutron detector has been in use since 2015. Its principle is identical to the one described for NEBULA, but its geometry and characteristics are different. NeuLAND is made of 400 plastic scintillator bars of dimensions $50 \times 2000 \times 50\,mm^3$ organized in eight successive layers of 50 bars oriented alternatively vertically and horizontally. The higher granularity of NeuLAND compared to NEBULA allows a better resolution on the position of the interaction and therefore on the reconstruction of the neutron four-momentum.

NEBULA+NeuLAND configuration

Simulations and estimates of the single detectors and their combination shows that NEBULA efficiency ϵ for the detection of one neutron is about 40%, with a measured resolution of about 6 cm in position and 120 ps in time.

In combination with NeuLAND, ϵ is around 50% for a single neutron. However, the efficiency drops with the number of neutrons and then, as reported in Sec. 1.3.1, the detection efficiency of 3n and 4n are estimated to be 8% and 0.7%, respectively, for $E_{decay} = 1\,MeV$ following phase-space decay. This ensures a 5 times higher total detection efficiency for the MIM method than the invariant mass one.

2.2 MINOS

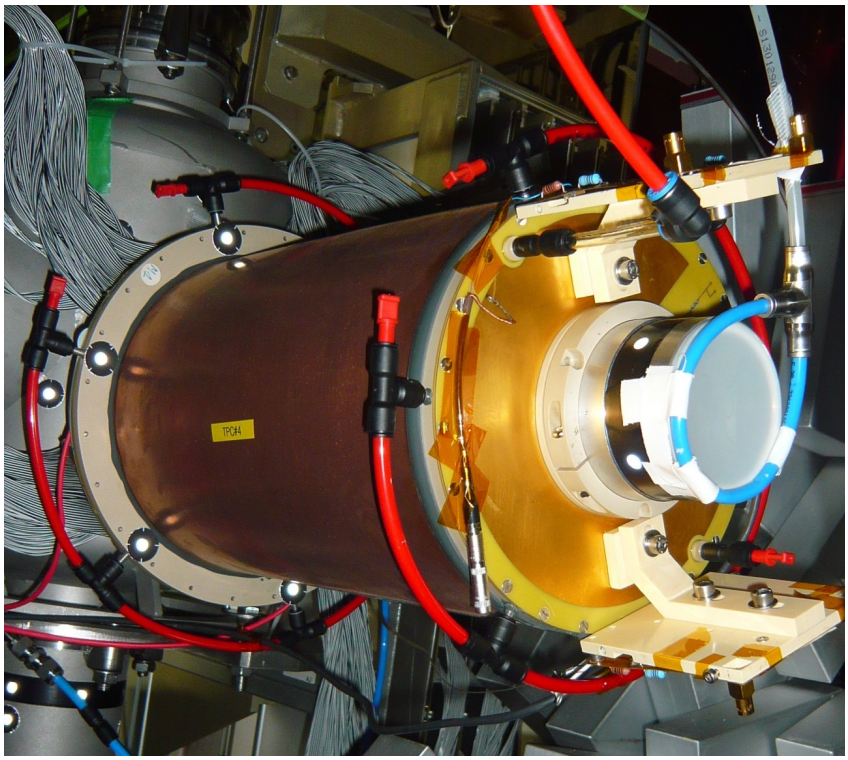

Figure 4: View of the MINOS TPC. The beam direction is from left to right. Courtesy by V. Lapoux, CEA.

MINOS (MagIc Numbers Off Stability), built in 2014 at the Commissariat à l'Energie Atomique et aux Energies Alternatives (CEA) in France, is composed of a **liquid hydrogen (LH_2) target** and surrounded by a **time projection chamber (TPC)**. This device is very useful for **proton-induced nucleon knockout** experiments and for this MINOS plays a central role in the study of neutron-rich nuclei at and beyond the neutron drip line.

MINOS allows the **tracking** of the reaction products and therefore makes it possible to determine the **interaction vertex**. It has the advantageous geometry of being free, in the frontside, by the LH_2 filling support as shown in Fig. 5. In this way it can efficiently be surrounded by several different types of detectors, ensuring a large solid angle coverage especially at very forward angles.

2.2.1 Target

The target is a cylinder of 3 cm diameter and its thickness could be adapted depending on the experimental requirement from 5 to 15 cm. To modify its thick-

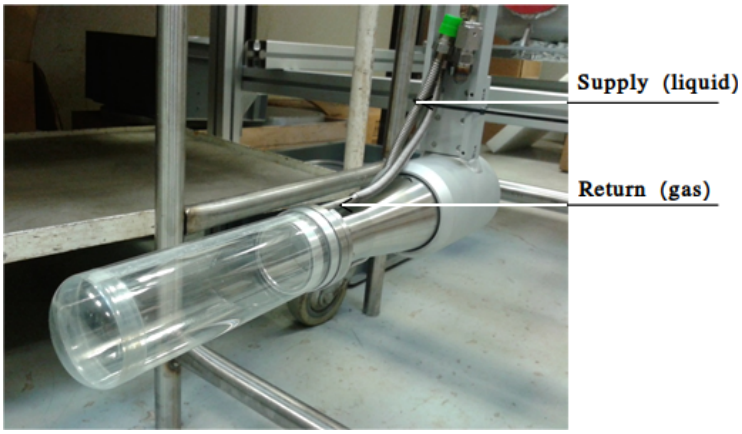

Figure 5: Front view of the target cell mounted on its aluminium support with the supply and exhaust tubes for hydrogen. The beam direction is from right to left. Courtesy by C. Santamaria.

ness it is sufficient to properly change the cylindrical window. The LH2 was kept at about 20 K with a density of 72.9 g/L^3. For our calibration and experimental runs the thickness was set at 150 mm, due to the curvature of the exit window and due to pressure and cryogenic effects, the length increased by 2.7 mm.

2.2.2 Time Projection Chamber

The MINOS target without its TPC cannot generally be used in standard in-beam gamma or invariant mass measurements because of its thickness. For that purpose, the vertex tracker, a time projection chamber (TPC), was developed to be positioned around the target. The goal of the TPC was to determine the vertex of the reaction with a precision better than 5 mm (FWHM) and to achieve a total detection efficiency better than 80% for both protons from a (p,2p) reaction.

The Time Projection Chamber is a hollow cylinder with inner and outer diameters of 4.1(1) and 9.1(1) cm respectively, and a length L_{TPC} =300(1) mm. The TPC is usually filled with a **special gas mixture** –Ar-iC_4H_{10}(3%)– that is a compromise between two basic characteristic for the performance of the detector, i.e.

- electron transverse and longitudinal diffusion,
- electron drift velocity and gain.

For MINOS the gas mixture was improved with respect to the standard one in order to have a higher drift velocity. This was obtained by adding 15% of CF_4 to the detriment of the percentage of argon. Figure 6 shows the simulations made by C. Santamaria. [San15, p. 17]

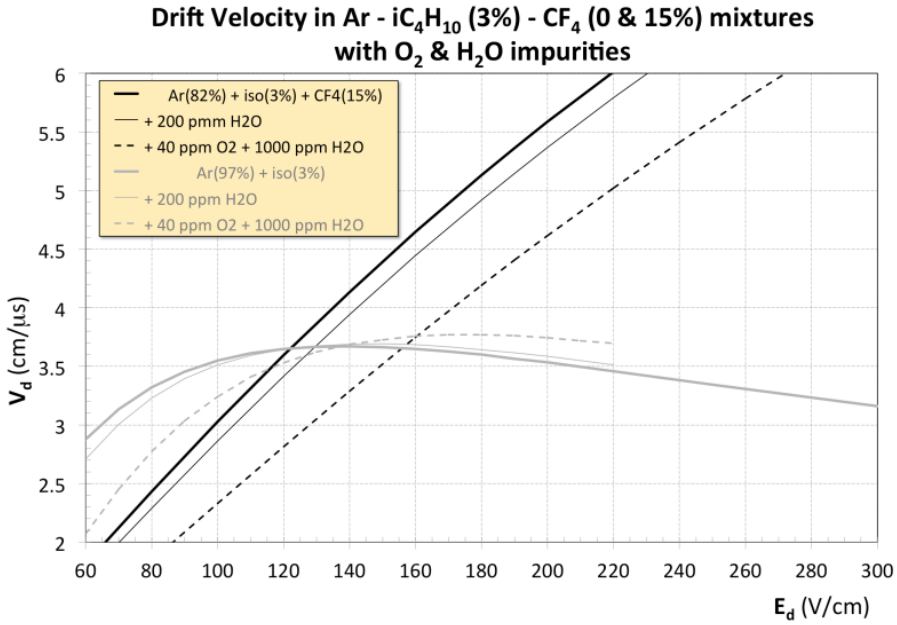

Figure 6: Simulations of the electron drift velocity as a function of the drift electric field for different gas mixtures.

Charged particles, passing through the gas of TPC, ionize the gas and generate free electrons. A **homogeneus** and **constant electric field** (E ~200 $V\,cm^{-1}$) is applied to drift these electrons towards the detection plane.

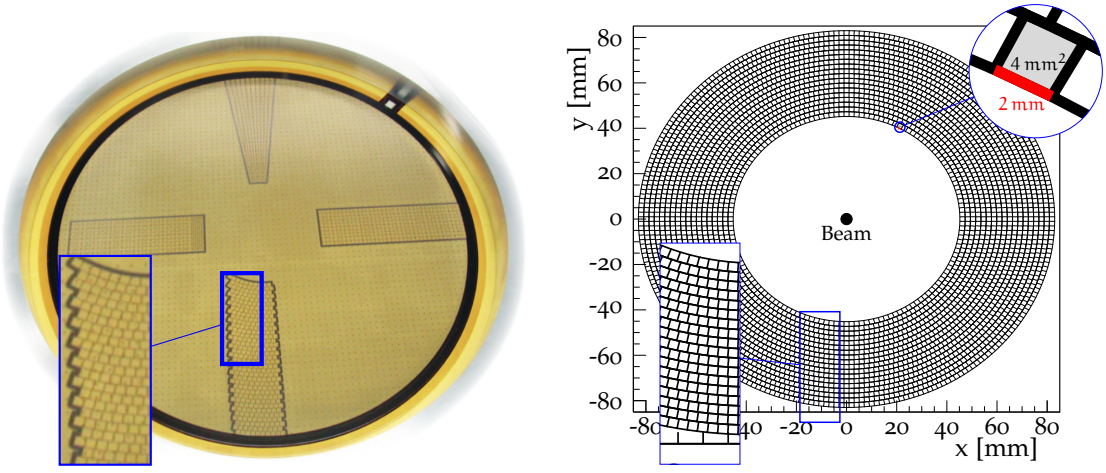

Figure 7: (Left) Photo of a bulk-micromegas detector segmented in pads in several methods. The zoom-in is for the segmentation kind used. (Right) Technical picture of pads distribution in 18 concentric rings.

The uniformity of the electric field reaches a value around of $\frac{E_x}{E_z} < 10^{-4}$. At the collector plane the electron signal is amplified in a bulk-micromegas detector segmented in pads. These are based on the PCB (Printed Circuit Board) technology [Gio+96; Gio+06]. There are in total **3604 pads** in the anode plane. Their size is quite constant (surface~4 mm^2) and they form **18** concentric **rings**. The partition of the pads is tabulated in Table 1 and a technical picture of the pad distribution is given in Fig. 7. The inner and outer radii of the detectors circular crown are 45 and 83 mm, respectively.

Table 1: Partition of the 3604 pads in the rings. The ring number 1 is the innermost and the number 18 is the most external.

Ring	# Pads	Ring	# Pads	Ring	# Pads
1	144	7	184	13	224
2	152	8	192	14	228
3	156	9	196	15	236
4	164	10	204	16	244
5	172	11	212	17	248
6	176	12	216	18	256
				TOT	3604

2.3 DALI

The Detector Array for Low Intensity radiation (DALI) array was originally designed for γ-ray detection by Rikkyo University and began operation in 1992, but part of it was used here for the proton detection.

The array was made up of 68 NaI(Tl) crystal detectors, and it was used to perform in-beam γ-ray spectroscopy experiments with techniques such as Coulomb excitation, inelastic scattering and breakup reactions. A new generation of this array, namely DALI2, was designed for in-beam γ-ray spectroscopy experiments using fast RI-beams and with a solid angle coverage of about 90% of 4π sr. DALI2 was developed from 2002 using 160 NaI(Tl) detectors[3], part of which from the original array. [Tak+14]

36 NaI(Tl) spare **crystal** detectors, made by the same manufacturer St. Gobain, were used to compose this array in 2017.

3 The crystals were manufactured by SAINT-GOBAIN and by SCIONIX, and their sizes are $45 \times 80 \times 160\ mm^3$ and $40 \times 80 \times 160\ mm^3$ for the two different types, respectively.

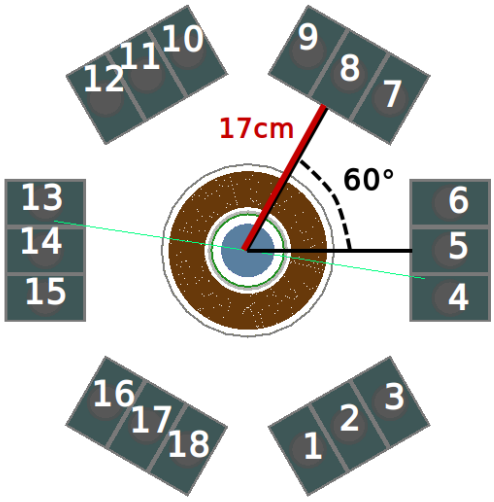

Figure 8: Frontal view of DALI: the relative angle between the triplets is shown, and the detector numbers are in white. The central orange circular crown is the pad plane and the blue circle is the target. One incoming proton and its nuclear reaction in the target are simulated in green.

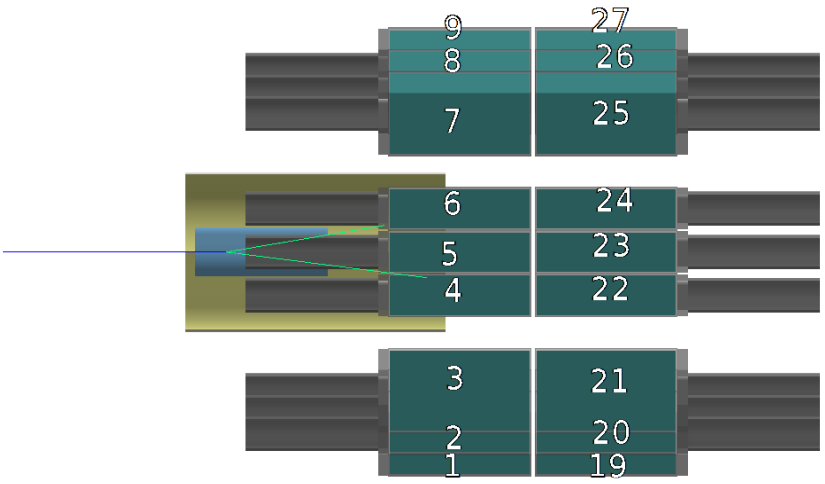

Figure 9: Lateral view of DALI: in yellow the MINOS tracker with inside the blue volume of LH2; in sea-green the NaI crystals with the gray PMTs. The detector numbers are written. One incoming proton (in blue) and its nuclear reaction (in green) in the target are simulated.

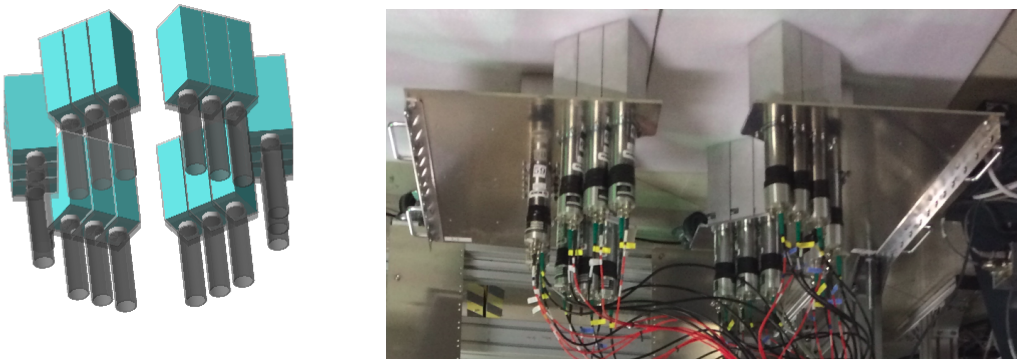

Figure 10: Comparison of one DALI ring in simulation and real photo. In the latter the two half-rings are occasionally spaced.

The crystals used in this array measure $45 \times 80 \times 160\,\mathrm{mm}^3$, covered by a 1.4 mm layer of manganate oxide MgO and by 1 mm of aluminium. Each scintillator was coupled to a 38 mm diameter HAMAMATSU R580 photomultiplier tube (PMT).

The crystals were then arranged in a suitable geometry to detect charged particles emitted by the reactions of interest, precisely in **two rings** around the beam axis. As shown in Fig. 8, each ring is composed of **6 triplets of crystals** positioned at intervals of 60° around the beam axis. The distance of the triplets from the beam axis is 17 cm.

3 GEANT4 SIMULATION AND COMPUTER TOOLS

In order to compare the calibration data and the experimental results, I developed a simulation of the MINOS and DALI devices using the framework **NPTOOL** [Mat+16] based on GEANT4 [Ago+03] and ROOT [BR97] toolkits. This allows to take into account the geometry and the materials of the experimental setup to make accurate predictions for this and following experimental campaigns.

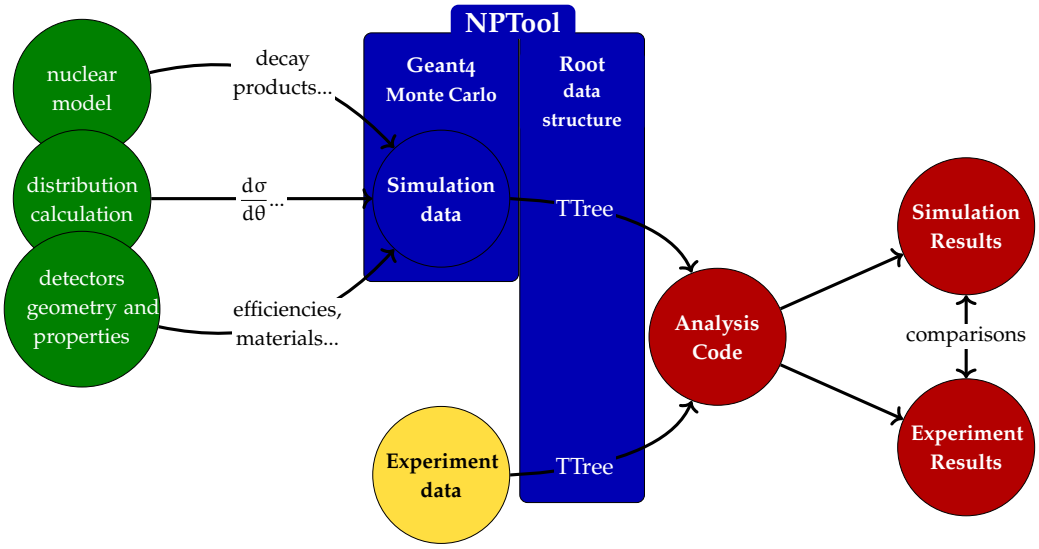

Figure 11: Schematic description of experiment and simulation data processing.

The two virtual arrays are **easily accessible** through this framework, even individually, and adjustable to the proper geometry setup. The advantages are also the **common uniform structure** of the generated ROOT trees, and the possibility to analyze with the same codes the experiment data and the simulation one. In fact, NPTool proposes a standardization of the organization also of the experimental data, through a conversion of them into the NPTool trees.

A scheme of the experimental and simulation data processing using NPTool is given in Fig. 11. The generated random events follow the nuclear model (e.g. a calculated cross section) given as input, and they are processed according to the experimental hypothesis (e.g. intrinsic efficiency and resolution of detectors) and known geometrical setup. The ROOT tree generated is analysed by the same code used also for experimental data.

3.1 RUNNING THE SIMULATION

The simulation program takes two input files. The first one, `xxx.detector`, is describing the geometry of the detector setup, and includes information such as position, material and target. The second one, `yyy.reaction`, is describing the kind of physics that should be simulated, whenever a source or a reaction, including information of the beam.

We can run the simulation by providing these two plain ASCII files using the following command:

```
npsimulation -D xxx.detector -E yyy.reaction
```

By default the program will search for these files, first in the local directory, typically the project folder $NPTOOL/Projects/$DET_NAME, and, if not found, will search in the $NPTOOL/Inputs folder which contains many standard files.

3.1.1 Detector configuration

The configuration input file has personalized keywords for each detector. In case of the Dali detector module, a simple example is shown in Fig. 12 resulting by the following lines:

```
%%%%%%%%%%%%%%%%%%%%%%%%%%%%%%%%
Target
 THICKNESS= 20 mm
 RADIUS= 20 mm
 MATERIAL= CD2
 ANGLE= 0 deg
 X= 0 mm
 Y= 0 mm
 Z= 0 mm
%%%%%%%%%%%%%%%%%%%%%%%%%%%%%%%%
Dali
 R = 212.4 mm
 Alpha = 120 deg
 Zeta = -90.03 mm
 Shape = Square
 Material = NaI_Tl
%%%%%%%%%%%%%%%%%%%%%%%%%%%%%%%%
```

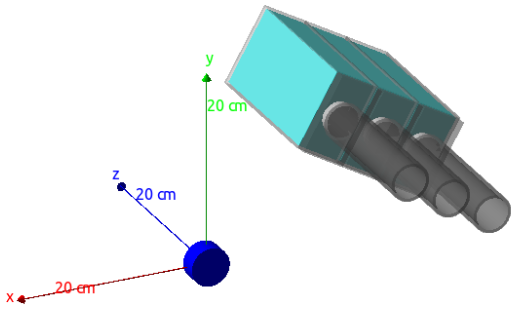

Figure 12: A triplet of DALI originated by the simple input file. An example of target is put in the middle in blue.

where the first block defines the size and the position of a target, and the second defines a triplet of crystals.

In order to declare a triplet of crystals in NPSimulation, the key word **Dali** should be specified in the geometry file. It should then be followed by the set of keywords, which is used to place the detector in the *world volume*, according to the Geant4 terminology.

The standard positioning of detectors in NPTool was in Cartesian or spherical coordinates, and I added the cylindrical one to permit this new class of configuration. In this case **R** defines the radial distance between the center of the detector and the z-axis, **Alpha** is the azimuth angle, i.e. the angle between the x-axis and the detector in the x-y orthogonal projection, and **Zeta** is the axial coordinate of the center of the detector. It is also possible to change the material of the crystals.

For Minos, I kept the possibility to use the classical positioning in Cartesian or spherical coordinates, but I added the variable **TargetLength**. This feature permits to easily change the size of the LH2 target of Minos. In the following example, the position is determined by Cartesian coordinates **POS**, which have the priority in the reading of commands, otherwise the spherical coordinates are used.

```
%%%%%%%%%%%%%%%%%%%%%%%%%%%%%%%%
Minos
  R= 0 mm
  THETA= 0 deg
  POS = 0 0 -50 cm
  PHI= 0 deg
  TargetLength = 152.76 mm
%%%%%%%%%%%%%%%%%%%%%%%%%%%%%%%%
```

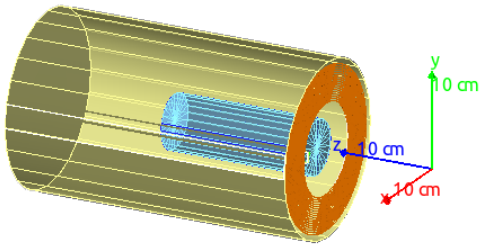

Figure 13: The MINOS TPC originated by the simple input file. The target is the blue cylinder and the plane with the micromega detectors is the red circular crown.

It is important to emphasize that the position refers to the target center, and in the simulation code there was a displacement of 11 mm between the beginning of the TPC and the target. This estimation was established after consultation of technical reports and improved after the analysis data explained in Sec. 5.4.6.

3.1.2 Event generator

The typical event generators used are: radioactive source, non-interacting beam and beam with a two-body reaction. The generator input file has personalised keywords for each reaction dynamics. The two following examples show the rather simple code needed to define the particles, energies, positions and directions.

```
%%%%%%% Isotropic source %%%%%%%
Isotropic
 EnergyLow= 0 MeV
 EnergyHigh= 25 MeV
 HalfOpenAngleMin= 0 deg
 HalfOpenAngleMax= 90 deg
 x0= 0 mm
 y0= 0 mm
 z0= 0 mm
 SigmaX= 0 mm
 SigmaY= 0 mm
 Multiplicity= 1
 Particle= proton
%%%%%%%%%%%%%%%%%%%%%%%%%%%%%
```

```
%%%%%% Two-body reaction %%%%%%
%%%%%%%%%%%%%%%%%%%%%%%%%%%%%%
Beam
 Particle= 1H
 ExcitationEnergy= 0
 Energy= 180
 SigmaEnergy= 0.448
 SigmaThetaX= 0.01
 SigmaPhiY= 0.01
 SigmaX= 0.01
 SigmaY= 0.01
 MeanThetaX= 0
 MeanPhiY= 0
 MeanX= 0
 MeanY= 0
%%%%%%%%%%%%%%%%%%%%%%%%%%%%%%
TwoBodyReaction
 Beam= 1H
 Target= 1H
 Light= 1H
 Heavy= 1H
 ExcitationEnergyLight= 0.0
 ExcitationEnergyHeavy= 0.0
 CrossSectionPath= flat.txt CSR
 ShootLight= 1
 ShootHeavy= 1
%%%%%%%%%%%%%%%%%%%%%%%%%%%%%%
```

A new event generator has been implemented to facilitate the first calibration of Dali discussed later in Sec. 4.2. The explanation of this implementation will be given in the following Sec. 3.2.

3.2 COSMIC MUONS SIMULATION

A new event generator was implemented to favor the first calibration of Dali as shown in Sec. 4.2. It simulates the distribution of the cosmic muons falling at the ground level. At first attempts were made to simulate the $\cos^2$ angle distribution using the *inverse transform sampling*. This method consists of finding the transfor-

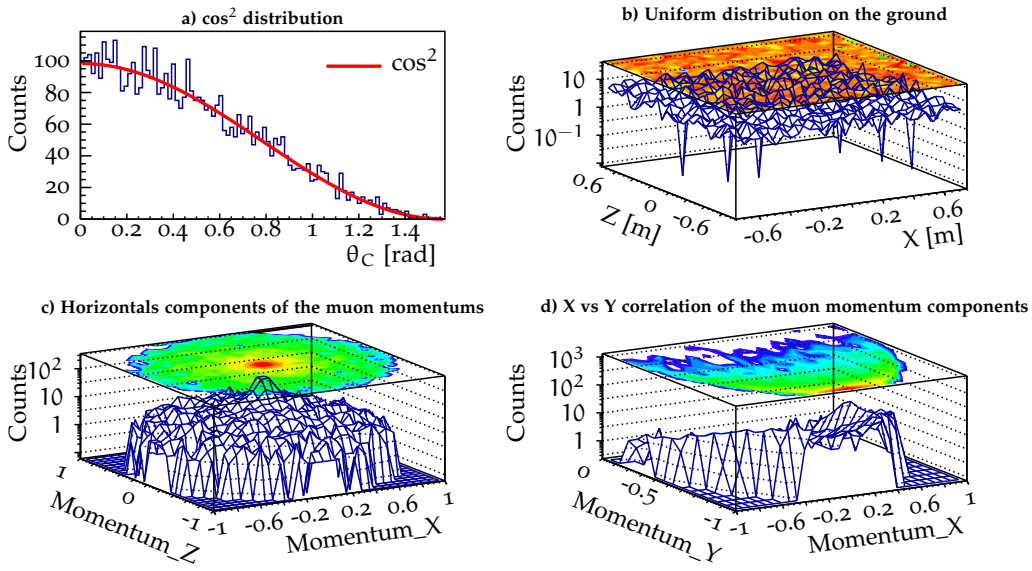

Figure 14: Cosmic distribution simulation: **a)** $\cos^2$ distribution of the muon angle θ_C originated by ROOT. **b)** Uniform distribution of muons on the horizontal plane at the DALI level. **c)** Distribution of the horizontal components of the muon momentums. The axis refer to the fraction of the momentum module. **d)** Distribution of the horizontal and vertical components of the muon momentums. The axis refer to the fraction of the momentum module.

mation function of primary random number in order to define a desired density distribution. The equation describing that is:

$$f(h^{-1}(y)) \left| \frac{dh^{-1}(y)}{dy} \right| = g(y), \tag{3.1}$$

where

- y are the final random values, that in our case they are the angles;
- $g(y)$ is the desired density distribution, i.e. the $\cos^2$ distribution;
- h is the unknown variable, called *transformation function*, we need to calculate;
- $f(h^{-1}(y))$ is the distribution of primary random numbers, i.e. usually the constant 1, which corresponds to the random values of Uniform(0,1).

In this approach the issue is the non-invertibility of the integral of the desired distribution ($\cos^2$). Also handling the equation with different primary random number distributions the issue was not solved.

To obtain the desired distribution the random generator by a ROOT function was included, obtaining the $\cos^2$ distribution (see a. of Fig. 14).

In order to use this angular distribution, we tried to optimize the useful events generation. For that a virtual square was defined in the X-Z plane at the DALI

level $y = 0$ and centered in $(x = 0, z = 0)$. The side of the square was $L = 1.5\,m$. For each generated event the algorithm to define the momentum versor (m_x, m_y, m_z) was the following:

- energy assignment to the particle;
- calculation of a random cosmic angle θ_C that respects the $\cos^2$ distribution. The value $\tan\theta_C$ will correspond to the ratio $\frac{m_x^2 + m_z^2}{m_y^2}$;
- calculation of a random angle φ_C that respects the uniform distribution from 0° to 360°. The value $\sin\theta_C$ will correspond to the ratio $\frac{m_x}{m_z}$;
- calculation of the momentum versor (m_x, m_y, m_z) using the energy, θ_C and φ_C values;
- selection of a random position (x, z) in the virtual square, that respects a uniform distribution;
- calculation of the initial position of the particle to be generated using the momentum versor and constraining the production in a common X-Z plane at level $y = 3\,m$.

This guaranteed the generation of useful events passing through the detector. In Fig. 14 the result distributions are checked.

4 DATA ANALYSIS OF DALI

The use of the DALI crystals in this experiment was not the standard one. In fact, for the purpose of the invariant mass and MIM methods in the analysis (cfr. Sec. 1.3.1), the goal of combining MINOS and DALI is the reconstruction of the knockout proton directions and their energies in the reaction vertex within the LH2 target.

Therefore, it is necessary at first to make a preliminary calibration using the cosmic rays, and then to proceed to a more refined one based on the proton-proton elastic scattering, that we collected in some experimental runs. Indeed thanks to the cosmic rays, we can tune several detectors to a common energy scale, and then the p-p scattering study will give the correct correlation between the detection in the crystal and the original energy of the particle in the target.

In the following sections at first the light output response of the detectors is studied, then the calibration process is described, with the several considerations and simulations.

4.1 LINEARITY OF NaI CRYSTALS

In 2017 at CYRIC (CYclotron and RadioIsotope Center in Tohoku University, Japan) the NaI crystals were tested with an 80 MeV proton beam to prove their use for the **detection of charged particles**. In these 7 tests the experimental energy resolution was better than 2%, except in one test where the measurement could have been affected by beam instabilities.

As we will discuss in Sec. 7.2, the light output of a scintillator depends on the kind of radiation detected and the risk of a non linear response was studied in [Ana+98]. In our case the **light output linearity** was successfully proved using some foils of aluminium as degreaders, and taking 3 different conditions:

- 80 MeV using directly the beam;
- 57.0 MeV obtained with 10 mm of Al and 1 mm of plastic;
- 41.1 MeV obtained with 16.2 mm of Al and 1 mm of plastic;

and the results are shown in Fig. 15. In this graph the light output and the beam energies are in the x and y axis, respectively. The light output was measured by

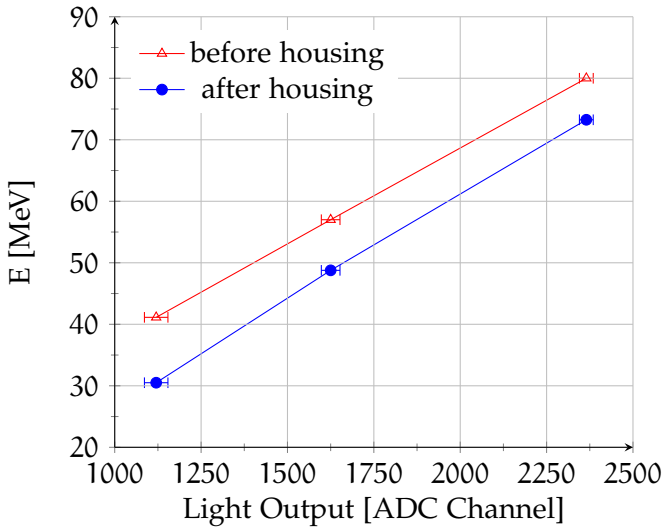

Figure 15: Linearity of the light output of NaI crystals in the energy region from 30 MeV to 80 MeV. The correct correlation, including the MgO layer: in red using the estimated energy of the incoming protons; in blue using the estimated energy of the protons inside the detector.

channel numbers, whereas the beam energies were obtained taking into account the energy loss calculated in the degreaders and materials. These estimates were made using the SRIM toolkit [ZZB10] inside LISE++ [Baz+02]. The blue data points in the graph correspond to the beam energy after the crystal housing. We considered in the analysis the effect of a 1 mm of aluminium Al and a 1.4 mm manganate oxide (MgO) layer on the inner surface of the aluminium housing. To provide the reader an idea about the correction, due to the energy loss in the (Al+MgO) housing, that one will have subsequently to account for the reconstruct the incoming proton energy, we report also in Fig. 15 the proton corresponding energies without the housing (red triangles). The good linear response of the crystals was confirmed. The different results between these measurements and those of the report [Ana+98] are due to the larger size of our scintillators, which avoid saturation effects typical for very small crystals (cfr. Sec. 7.2).

4.2 CALIBRATION BY COSMIC RAYS

Ascertained the linear response of the crystals, the first calibration of the detectors was much simpler using linear relationships. For this calibration we used cosmic rays and we exploited the geometry of the crystals and the array to do this.

As shown in Fig. 16, in a NaI crystal different injection trajectories release different energies. For each path the **interaction length** is written close to the arrow.

In order to select specific paths and their corresponding energy peaks, **two coincidence methods** were adopted:

(a) Three crystals of the same detectors unit to identify the length of 4.81 cm, e.g. detectors 13-14-15.

(b) Two opposite detectors of the same ring to identify the length of 8.32 cm, e.g. detectors 7 and 18.

Some examples are shown in Fig. 17.

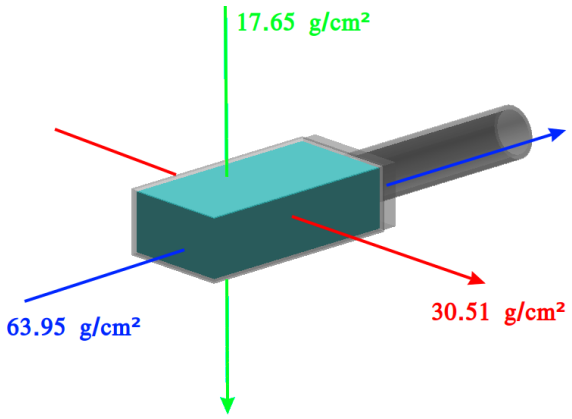

Figure 16: Several paths of a charged particle inside the crystal. The respective interaction length are written close to the arrows.

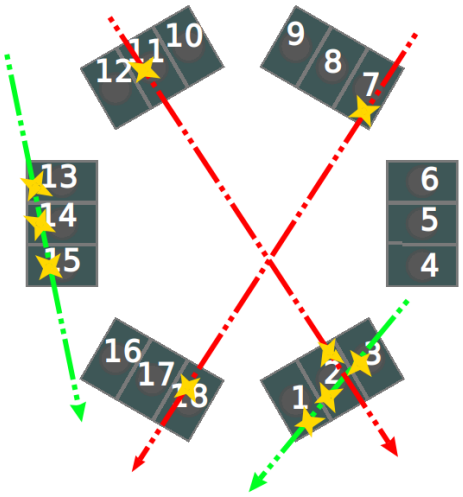

Figure 17: Possible coincidence methods to identify cosmic muons: in green the *detectors unit coincidence* (a), in red the *two opposite detectors coincidence* (b). Yellow stars indicate the activation of the detectors.

Theoretical estimation

At first, people on duty during the experiment made a rough estimation of the energies released for each path. They evaluated the energy loss at 25, 42, 87 MeV for the respective paths. Looking at the available bibliography, I established that those values were underestimated. I tried to calculate the values considering the hypothetical energy of muons and the material used.

It is known that the energy of the muons arriving on ground is around 4 GeV. The energy loss in the concrete of the laboratory building is 1.5 GeV, so at the laboratory level the muon energy is around 2.5 GeV.

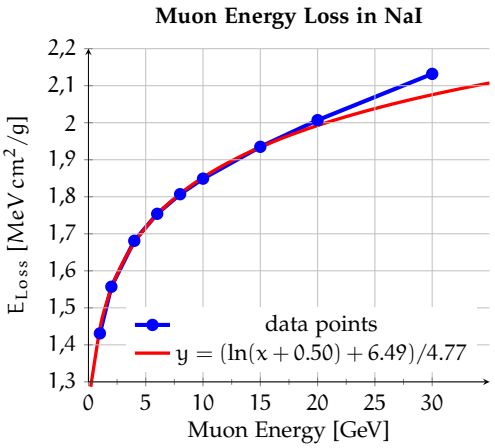

Figure 18: Dependence between the muon energy and the energy loss. Data points from [WL85] in blue and the fit in red.

The E_{loss} [WL85] is plotted in Fig. 18 as a function of the muon energy. Data points were fitted parameterized in according to a logarithmic behaviour. The obtained function was used to calculate the E_{loss} with a computational method. Given the initial muon energy and the path length inside the NaI crystal, the energy loss was calculated in 2 iterative steps:

- calculation of the energy loss in 0.1 mm steps as a function of the muon energy;
- subtraction of this partial energy loss from the particle energy and sum to a cumulative variable E_{loss}.

At the end of the calculation, we obtained the overall by the muon along the entire trajectory. The estimated value for a length of 4.8 cm in the NaI (i.e. 17.67 g/cm^2 due to the density of 3.666 g/cm^3) was 28 MeV, for 8.32 cm was 48.5 MeV, and for 17.44 cm we calculated 101.5 MeV.

Shape and fit of peaks

As explained at the beginning of this section, we used coincidence conditions between the detectors in order to select the helpful paths of muons through the crystals.

An example of the energy distribution for one detector is shown in Fig. 19. In order to perform the **peak identification**, we set the noise level at channel 320 of the ADC and we put a minimum threshold from which we considered the complete muon passage into the crystal, in order to decrease the background. To identify the 4 cm path (coincidence method (a) of Sec. 4.2) we set a threshold at ADC channel 350, on the other hand, for the 8 cm path (method (b)) the threshold was set at channel 600.

We can compare the different energy spectra originated by the coincidence methods thanks the **2D-matrices** in Fig. 20-21. The x-axis refers to the DALI detector number, and the y-axis to the detected energies in ADC channels. In Fig. 20 the lighter spots correspond to the detector units in vertical positions, for which more muons passed. On the contrary, in Fig. 21, those detectors had no statistic in the *two-opposite coincidence*.

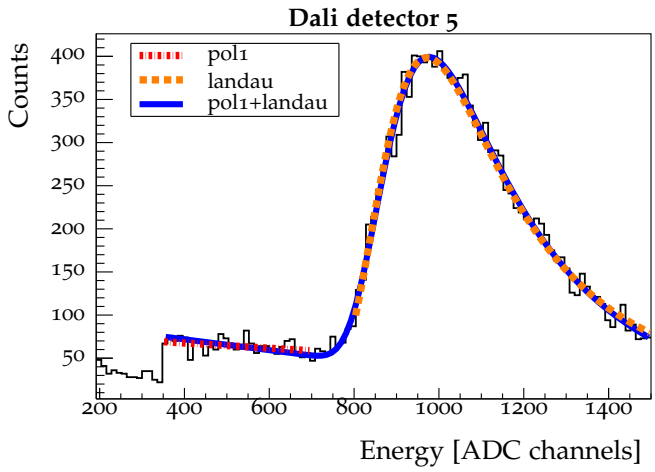

Figure 19: Fit of the energy peak in the Dali crystal number 5 using the coincidence method (a). In red the partial fit with pol1, in orange the p. fit with landau, in blue the total fit with pol1+landau function. Threshold for the coincidence method set at the adc channel 350.

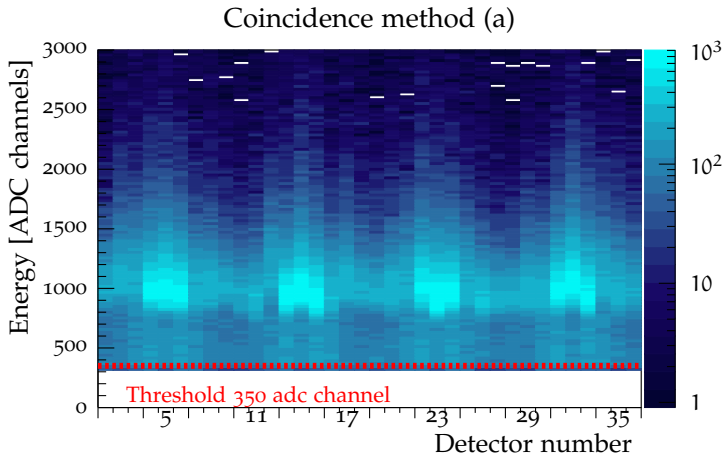

Figure 20: Energy spectra for DALI detectors in *triplet coincidence*.

For each crystal, the energy distribution displays at least a well defined peak, and the best function for its fit was studied. We compared several functions to find the best χ^2 value fitting a distribution sample:

Function[1]	χ^2
exp+landau	3.0
pol1+landau	1.5
pol1+gaus	8.9
moyal+pol1	3.6

1 where: **pol1** is the first degree polynomial function; **exp** the exponential function; **gaus** the gaussian function; **landau(x)** $= \frac{1}{\pi\sigma}\int_0^\infty e^{-t}\cos\left(t\frac{x-\mu}{\sigma}+\frac{2t}{\pi}\log\frac{t}{\sigma}\right)dt$; **moyal(x)** $= \exp\left[-\frac{1}{2}(c+\exp -c)\right]/\sqrt{2\pi}/b$ with $c=\frac{x-a}{b}$

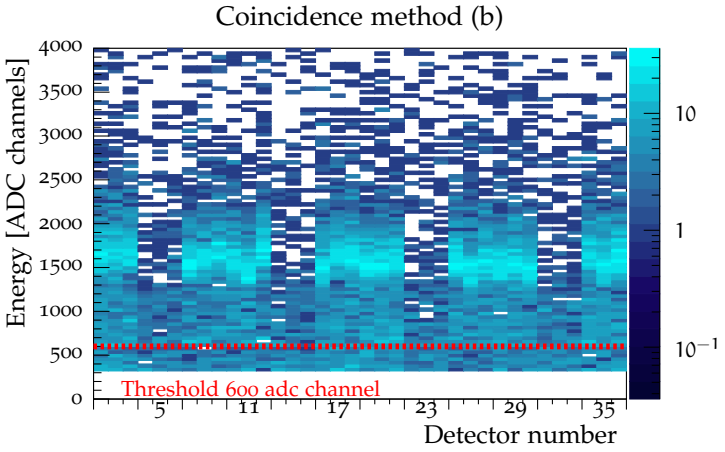

Figure 21: Energy spectra for DALI detectors in *two-opposite coincidence*.

According to a χ^2 analysis the combination **pol1+landau** was chosen to determine the peak of the energy released by muons.

We used also two acquisition runs made at the end of the experiment with two **calibration sources** (^{60}Co and ^{137}Cs). These runs were not important for the calibration of our experimental data, but they were only checks for the DAQ. The chosen functions fitting the photopeaks were:

- for ^{60}Co the combination expo+gaus+gaus for its 2 photopeaks;

- for ^{137}Cs the combination expo+gaus for its main peak and expo+gaus+gaus for the double photopeak of ^{137}Cs, i.e. the peak formed by the acquisition of 2 photons at the same time.

4.2.1 Simulation of the cosmic rays peaks

In order to take into account the geometry of the experimental setup and its consequences on the peak shapes, the simulation was implemented as explained in Ch. 3. The simulation data were processed with the **same** coincidence **algorithm**, and the results were finally used for the calibration.

In Fig. 22 the peaks of the simulations and the experiment data are shown. It was possible to determine the resolution of the detectors from this comparison, and it was important to have the distribution in the same energy range to compare the peaks. For this the simulation data were scaled to the acquisition range of the ADC, multiplying by a factor $F = \frac{\text{adc range position} \simeq 1000}{\text{energy peak position} \simeq 23} \simeq 44$.

At first, we simulated the detection with a "perfect" resolution, so the σ value of the landau function fitting the peak was only due to geometrical effects and to the stochastic nature of the energy loss.

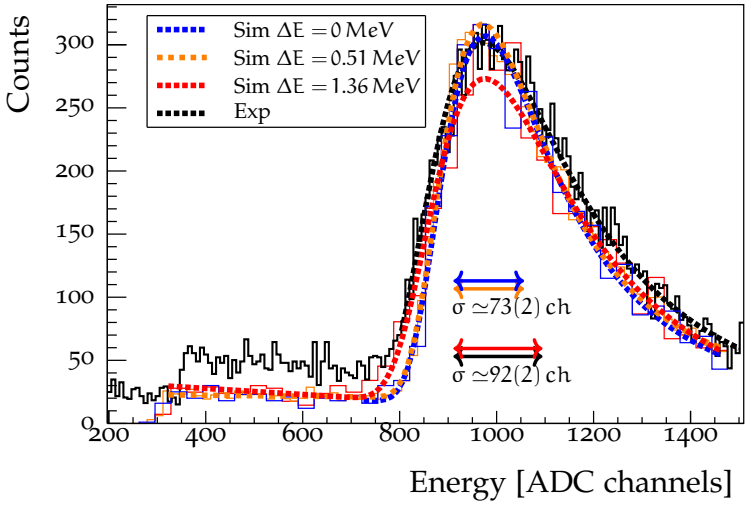

Figure 22: Comparison of the experimental and simulation peaks. The simulation data were suitable adjusted and shifted to the experimental peak position. The sigma values for the landau function were: $\sigma_{0/0.51} = 73(2)$ (blue and orange for "perfect" resolution or $\Delta E = 0.51\,MeV$, respectively) or $\sigma_{1.36/exp} = 92(2)$ (red and black, for $\Delta E = 1.36\,MeV$ or the experiment data, respectively). Motivations for the used resolutions are given in the text.

From the test made at CYRIC (cfr. Sec. 4.1), we knew the NaI crystals resolution $\Delta E = 1.36\,MeV$ for the proton beam at $80\,MeV$. This means a resolution of 1.7%, i.e. $0.51\,MeV$ for an energy release of around $30\,MeV$. Using the perfect resolution or ΔE =0.51 MeV, the obtained σ values were respectively $\sigma_0 = 74(3)$ and $\sigma_{0.51} = 72(1)$. These values were not compatible with that of the experiment data fit, in which $\sigma_{exp} = 92(2)$. On the contrary, this value appeared in the simulation with $\Delta E = 1.36\,MeV$ giving $\sigma_{1.36} = 92(5)$.

We established we had to use the crystal resolution $\Delta E = 1.36\,MeV$ for the following simulations.

Raw calibration by cosmic rays using simulation

A calibration program has been implemented in order to automatize the process for different muon energies or for the use of calibration sources.

The used conversion equation was:

$$E_{MeV} = Q_{cal}\left(E_{ch} - Q_{ped}\right),$$

where E_{MeV} is the energy in MeV, E_{ch} the energy in ADC channels, Q_{cal} the linear coefficient and Q_{ped} the intercept parameter. For detectors in "oblique"

positioning[2] a linear calibration was made using the two found peaks. The vertical detector units[3], with only one peak, were calibrated applying the average of the Q_{cal} values previously calculated, and Q_{ped} was obtained using the known peak. An example of the calibration programme output is shown in Fig. 23.

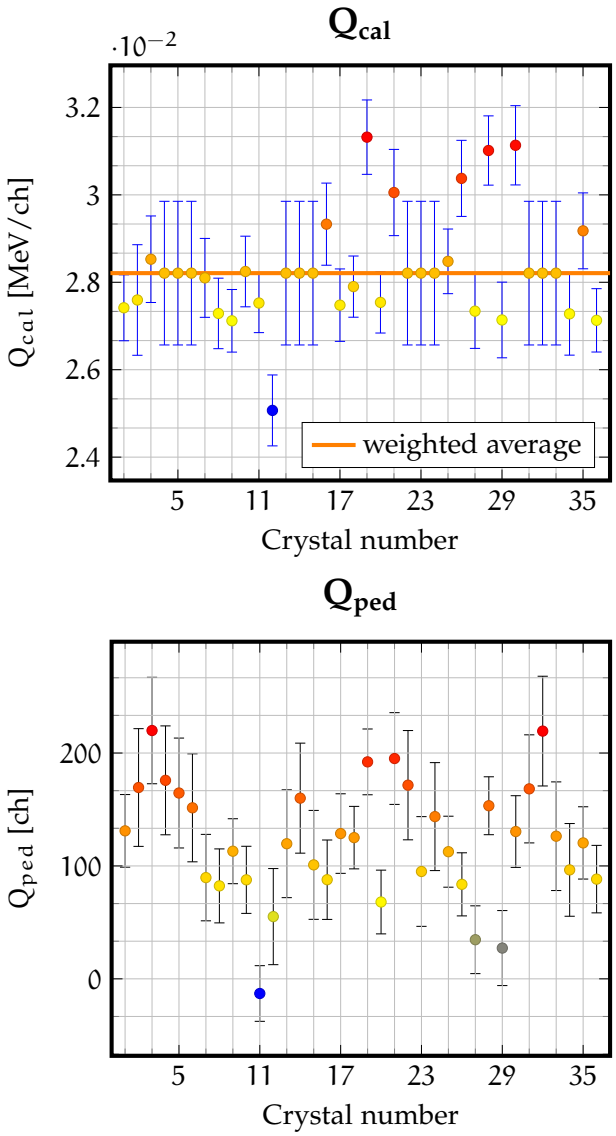

Figure 23: Linear coefficients values (top) and intercept values (bottom) for the calibration of the 36 crystals.

2 Triplets 1-3, 7-9, 10-12, 16-18, 19-21, 25-27, 28-30, 34-36 in Fig. 8-9.
3 Triplets 4-6, 13-15, 22-24, 31-33 in Fig. 8-9.

5 CALIBRATION OF MINOS

The MINOS device is used in order to reconstruct the tracks of the charged particles scattered from the target. This is needed to measure the momentum of these particles for the MIM method (cfr. Sec. 1.3.1), and to determine the point where the nuclear reaction took place, namely the reaction vertex, for both methods of mass reconstruction.

This chapter explains the different observables provided by the detector and the track identification method used. Hence, several analysis issues are described and a solution is given also thanks to some simulations.

5.1 DETECTION OF THE DRIFT ELECTRONS

In Sec. 2.2.2 we quickly described the working principle of our TPC. Charged particles pass through the gas and ionize it producing free electrons. These electrons generate a small flow in the opposite direction to the electric field. This phenomenon is called *drift*, and the electron velocity is named "drift velocity", v_{drift}. Similarly t_{drift} is the drift time between the gas ionization and the electron collection at the anode plane.

On average, 80 pads of the MINOS anode plane are triggered for each collected event. The detector pads correspond to precise positions (x, y) in the plane and each pad measures a Charge vs Time signal, shown in Fig. 24, from which the maximum charge value and a time t_{pad} correlated to the drift time, were extracted. The fit was based on the following equation:

$$q(t) = A \times e^{-3\frac{t-t_{pad}}{\tau}} \sin\frac{t-t_{pad}}{\tau}\left(\frac{t-t_{pad}}{\tau}\right)^3 + q_b$$

where τ is a exp decay time value, q_b is the baseline, and A a scaling factor.

The data acquisition was set using the polygonal histogram corresponding to the pads layout. The minimum charge detected by pads was around 30 adc channel in one entire run, but the average of minimum charge in the tracks was around 250 adc channel. The current analysis algorithm used for the pads did not present a software threshold, as the hardware threshold were set high enough to remove any significant noise. Some event examples are shown in Fig. 25. Note in the example at right the detection of two delta electrons, one per track. This kind of electron is originated by an high excitation of the gas electrons and not by the

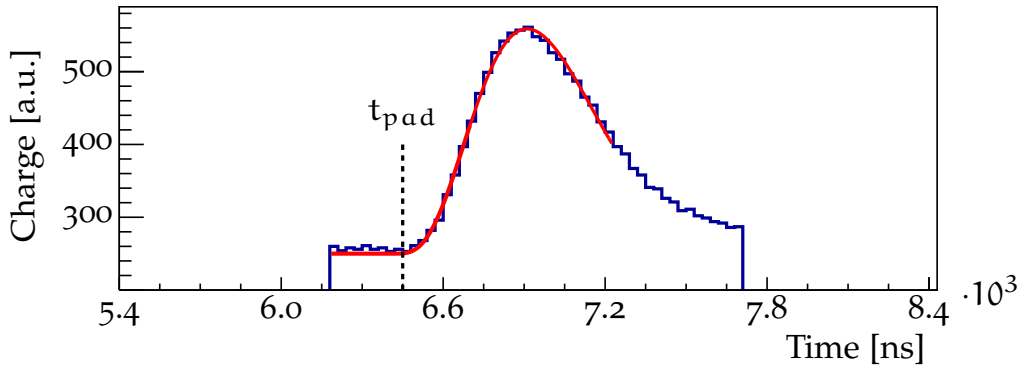

Figure 24: Example of the charge vs Time signal analyzed for each pad. In red the fitted function extracting the t_{pad} value.

usual ionization. As explained in Sec. 5.3, this noise is efficiently removed by the track identification algorithm.

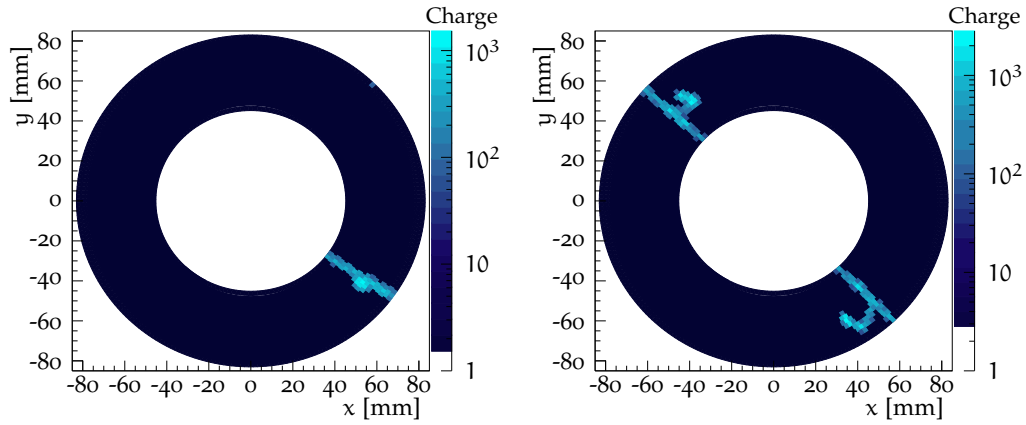

Figure 25: Examples of events in MINOS. The light lines correspond to the pads activated by the drift electrons. At left only one track can be reconstruct, at right two tracks are shown, each of them presents a delta electron contribution.

5.2 DETERMINATION OF DRIFT VELOCITY

In order to determine the ionization positions for the track reconstruction, it is necessary to know the (x, y) information and the location along the TPC length where the reaction occurred. For this, the z value is extracted from the t_{pad} and v_{drift} values as explained in Sec. 5.3. The t_{pad} is measured almost directly, on the contrary, v_{drift} needs a little longer procedure. The method for its determination and use is now provided.

The first step, in the standard approach [San15, p. 42] to calculate the v_{drift}, is to plot a time distribution of all the collected t_{pad} values in an acquisition run. An example of this distribution for p-p scattering is shown in Fig. 26. Hence the minimum and maximum times, called T_{Start} and T_{Stop}, respectively, are determined for each run.

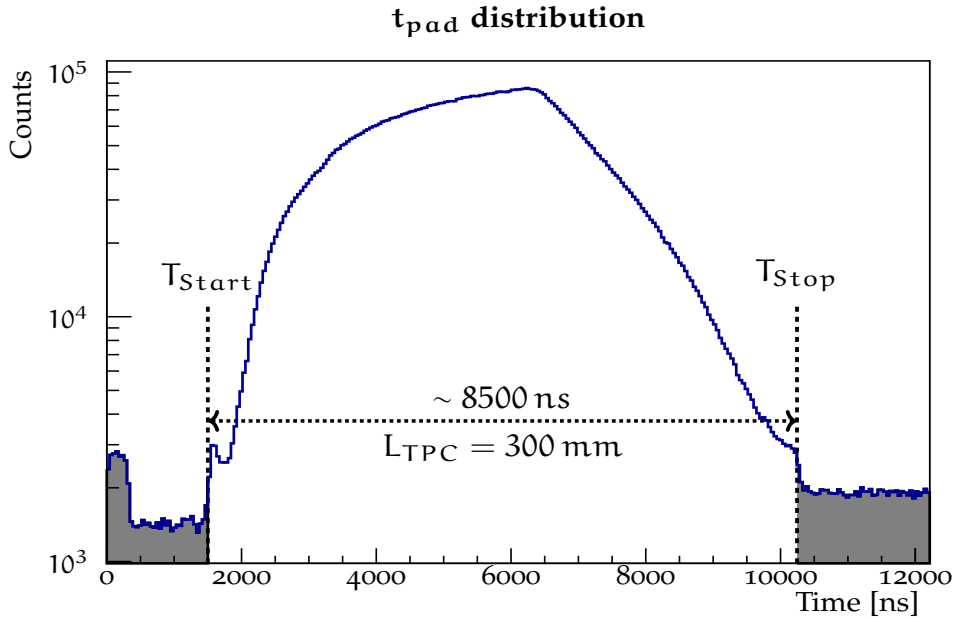

Figure 26: Distribution of the t_{pad} values obtained from the detection signal analysis. The beginning of the distribution is defined as T_{Start}, the end as T_{Stop}. The noise is in gray.

This protocol for the measurement of v_{drift} is based on the assumption that T_{Start} and T_{Stop} are correlated to the measurement of the electrons generated at the beginning (upstream) and at the end (downstream), respectively, of the active TPC volume of geometrical length $L_{TPC} = 300\,mm$.

This means that the natural solution is:

$$v_{drift} = \frac{L_{TPC}}{T_{Stop} - T_{Start}}. \tag{5.1}$$

The T_{Start} point was supposed to be constant during all the experiment. We looked at this value for both the proton and ^{8}He beam data sets and found compatible values. The parameter was also related to the mean delay between the time signals from the trigger and the detection pads. Therefore its contribution was important also in the next step of the analysis, as explain at the end of Sec. 5.3.

In Fig. 27 we observe the T_{Stop} position was changing, i.e. a change in v_{drift} was occurring. These changes could be originated by various factors, such as for instance fluctuation of E_{field}, changing of the gas pressure or impurities. The

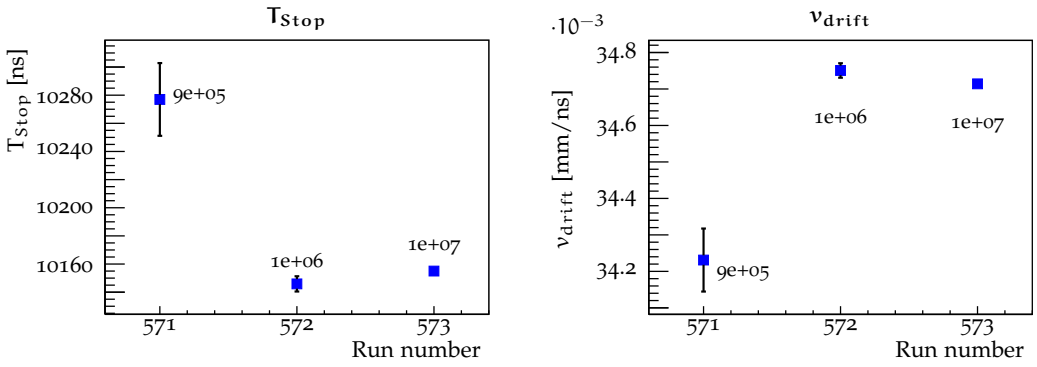

Figure 27: Identification of the T_{Stop} position (at left) and the v_{drift} value (at right) for the acquisitions with the proton beam.

numbers close to the data points are the number of events used to determine the T_{Stop} values, and for these measures we note smaller and smaller errors with the increase in statistics.

Applying this method the mean value measured was around $0.0345(2)\,mm/ns$. The value was smaller than that expected and measured in previous experiments using MINOS, the discrepancy was about $0.01\,mm/ns$, i.e. more than 20% lower. The presence of a large amount of impurities in the TPC chamber could motivate this difference. Comparing the experimental drift speed with the graph in Fig. 6, it would also be possible that the low speed was due to the use of a standard gas for the TPC maintaining the voltage level at $200\,V\,cm^{-1}$.

5.3 IDENTIFICATION OF PARTICLE TRACKS

The two coordinates of each pad and their associated drift times were put together to reconstruct a three-dimensional track of the particle. By finding the crossing of the different tracks within an event, we could reconstruct the reaction vertex inside the LH2 target.

In addition, the time has allowed us to reconstruct the missing z coordinate (along the beam axis) of the ionization position. The z_{pad} value is assumed to be proportional to the drift time by the following formula:

$$z_{pad} = t_{pad} \times v_{drift}. \tag{5.2}$$

In this way, z_{pad} corresponds to the distance between the anode plane and the ionization position in the TPC.

The technique used to convert the raw data to tracks in the TPC is based on the **Hough transformation** in the polar coordinate system [HV62]. Assuming that all

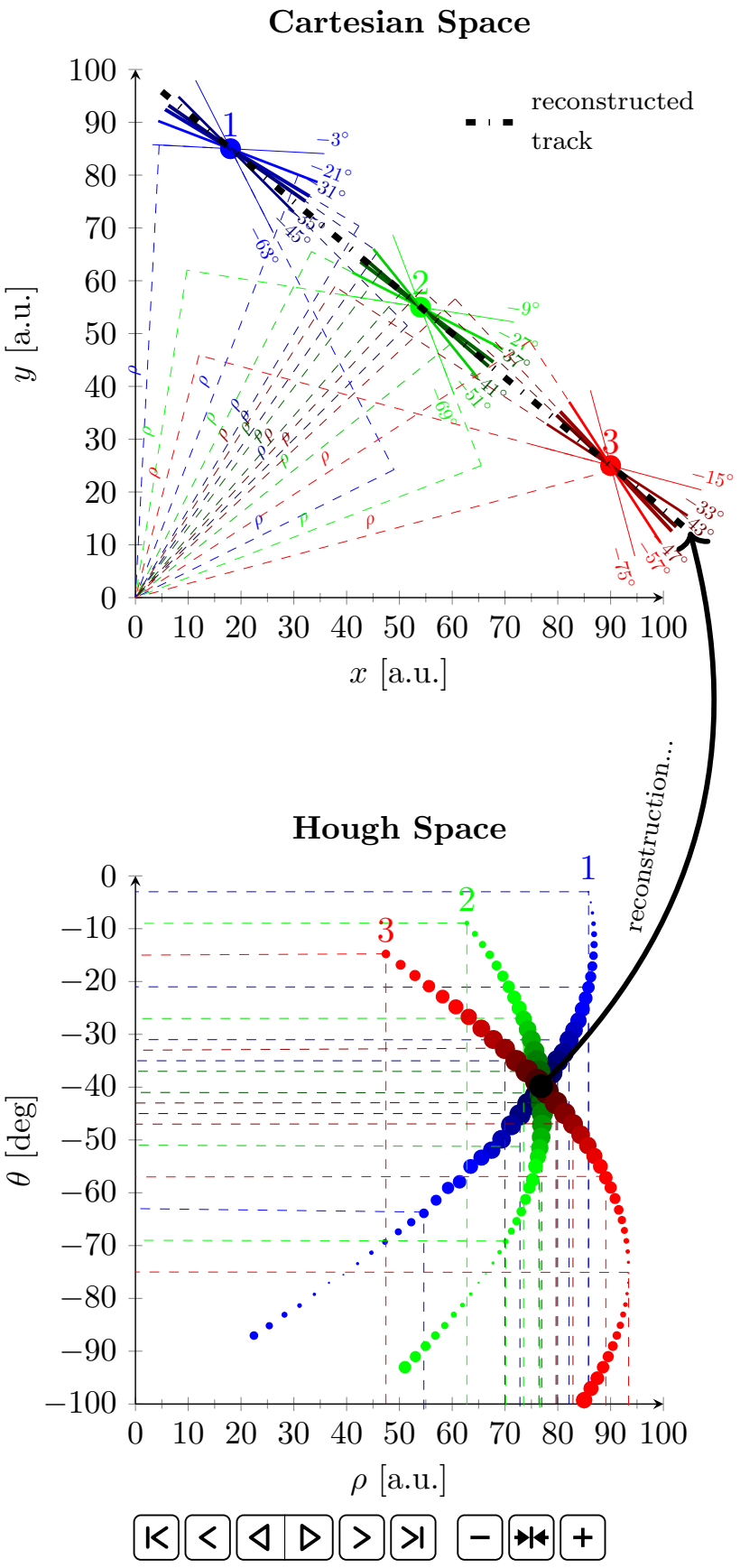

Figure 28: Hough transformation. The three colored points in the Cartesian space are processed in the Hough conversion. For each point a family of intersecting straight lines is generated, and these lines are associated to their (ρ, θ) values plotted in the Hough space. The track is reconstructed by the concentration in the Hough coordinates $(\rho = 77, \theta = -40°)$.

the points of a trace belong to the same direction, the goal is to recognize this direction in a computational way. Therefore, each point is assumed to be the center of a family of intersecting straight lines. Each line corresponds to the polar coordinates (ρ, θ), representing the distance (ρ) and the polar angle (θ) from the center of the reference frame. Filling a 2D-histogram of the Hough space with polar coordinates, obtained from each point of the trace, the final result will be a peak corresponding to the polar coordinate of the particle direction. In Fig. 28 an example with three points is given and in which, for convenience, the θ value refers to the straight line slope and not to the polar angle of its distance from the origin.

This reconstruction for Minos was basically divided into two steps: the 2D and the 3D Hough transformation. The first finds the track using the (x, y) information only, and identifies the pads belonging to this. The method in this step was improved for the specific configuration of the TPC. Detailed information about that is available in [San15, p. 36-37].

After that, knowing the drift speed in the gas, we obtained the third (z) dimension of our signals through Eq. (5.2), and a 3D Hough transformation is applied. Thus the analysis is made in the projection planes X-Z and Y-Z. Each of them gives the direction of the track in its own plane, and their combination provides the solution in three dimensions. In this reconstruction the data coming from delta electrons are excluded, in order to obtain cleaner tracks.

The tracks are therefore determined and their polar angles θ_p in the laboratory are calculated with $13\,\mathrm{mrad}$ resolution. For each couple of tracks the minimal distance $\mathbf{D_{min}}$ is calculated. The mid-point defines the reaction vertex in (x, y, z) coordinates. In case of more than two tracks reconstructed, those with the smallest minimum distance are used.[1]

The **vertex distribution** will be very important to know the reliability of the array and of the track reconstruction. Although usually, since to the mean delay between the time signals from the trigger and the pads was not taken into account in the t_{pad} measurement, then in z_{pad}, the final vertices positions are shifted along the z-axis to put the beginning of the target at the zero-point. Considering the data processing code, I established that, for a correct reconstruction, the delay (and then T_{Start}) has to be adjusted before the 3D Hough transformation, as explained in the previous section, and the Eq. (5.2) should be corrected into $z_{pad} = (t_{pad} - T_{Start}) \times v_{drift}$, or basing on the T_{Stop} value

$$z_{pad} = L_{TPC} - (T_{Stop} - t_{pad}) \times v_{drift}.$$

1 However this does not correspond always to our physical case, the proton knock-out. These events will be discarded in the following analysis.

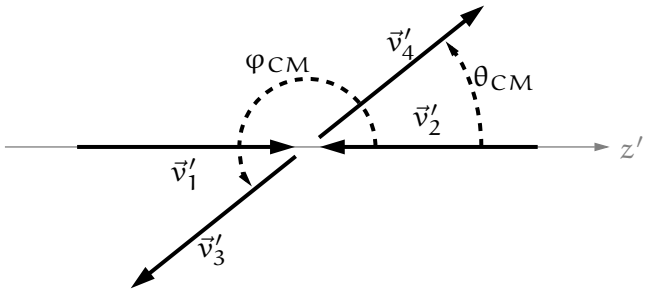

Figure 29: Two-body reaction in the centre-of-mass frame. The velocities of the projectile, $\vec{p}'_1$, and the target, $\vec{p}'_2$, and those of the products, $\vec{p}'_3$ and $\vec{p}'_4$, are displayed.

5.4 CALIBRATION USING P–P ELASTIC SCATTERING

As explained in Sec. 4, in order to definitively calibrate DALI it is necessary to combine it with the track directions offered by MINOS. Therefore, we analysed some runs during which a proton beam was used, and we took advantage of the p-p elastic scattering to finalize the calibration.

In fact, when one scattered proton is detected by DALI, its arrival energy to the crystal is known thanks to the previous calibration by cosmic rays. Then the original energy in the nuclear reaction vertex has to be reconstructed by adding the several energy losses in the materials, of which we know the interaction lengths by means of the MINOS tracking. After doing this, if the reconstruction procedure is correct, the sum of the proton energies should be the energy of the projectile proton in the reaction vertex.

5.4.1 Proton–Proton relative angle

The first step for the calibration via p-p elastic scattering was the control of a well-known observable of the two-body reaction: the relative angle of the products. Using the energy and momentum conservation, the relative angle in the laboratory frame was derived both for the non-relativistic and relativistic kinematics. In the following sections, both in formulas and in figures, the projectile and target are particles numbered with 1 and 2, respectively, while their products are marked with 3 and 4. Primed variables correspond to the centre-of-mass (c.m.) frame.

Non-relativistic approach

From momentum conservation in the c.m. frame

$$\vec{p}'_1 + \vec{p}'_2 = 0 = \vec{p}'_3 + \vec{p}'_4,$$

and in our particular case each particle is a proton with mass M=938 MeV. Hence, since

$$\vec{v}_1' + \vec{v}_2' = 0 = \vec{v}_3' + \vec{v}_4',$$

there are equal and opposite particle velocities both before and after the collision, with modules v_i' and v_f', respectively. Therefore also the centre-of-mass angles, θ_{CM} and φ_{CM} , of the outgoing particles have a 180° difference. Moreover, for the kinetic energy conservation of the elastic scattering

$$E_k^{initial} = E_k^{final} \quad \longrightarrow \quad 2 \cdot \frac{v_i'}{2M} = 2 \cdot \frac{v_f'}{2M} \quad \longrightarrow \quad v_i' = v_f'.$$

Fig. 29 supports the description of this kinematics.

The velocity in the laboratory frame is composed by the centre-of-mass velocity (in the laboratory frame) summed to the particle velocity in the c.m. frame. The composition

$$\vec{v} = \vec{v}_{CM} + \vec{v}'.$$

is shown in Fig. 30.

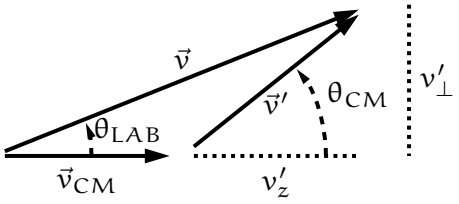

Figure 30: Composition of particle velocities from the centre-of-mass to the laboratory frame.

Let θ_{CM} be the angle of the particle motion relative to the z-axis in the c.m. frame. Then $v_\perp' = v' \sin\theta_{CM}$ is the velocity component perpendicular to the z-axis and $v_z' = v' \cos\theta_{CM}$ is the component along z. Hence the corresponding angle in the laboratory frame, θ_{LAB}, is determined from

$$\tan\theta_{LAB} = \frac{v_\perp'}{v_{CM} + v_z'} = \frac{v' \sin\theta_{CM}}{v_{CM} + v' \cos\theta_{CM}} = \frac{\sin\theta_{CM}}{\frac{v_{CM}}{v'} + \cos\theta_{CM}}, \qquad (5.3)$$

where the ratio v_{CM}/v' can be simplified for the equality of velocity modules.

Then for both particles:

$$\theta_{LAB} = \arctan\left(\frac{\sin\theta_{CM}}{1 + \cos\theta_{CM}}\right) \qquad \text{and} \qquad \varphi_{LAB} = \arctan\left(\frac{\sin\varphi_{CM}}{1 + \cos\varphi_{CM}}\right).$$

In order to explicit the relative angle θ_{PP} between the particles we use the subtraction property of the arctan function:

$$\arctan a - \arctan b = \arctan\frac{a - b}{1 + ab},$$

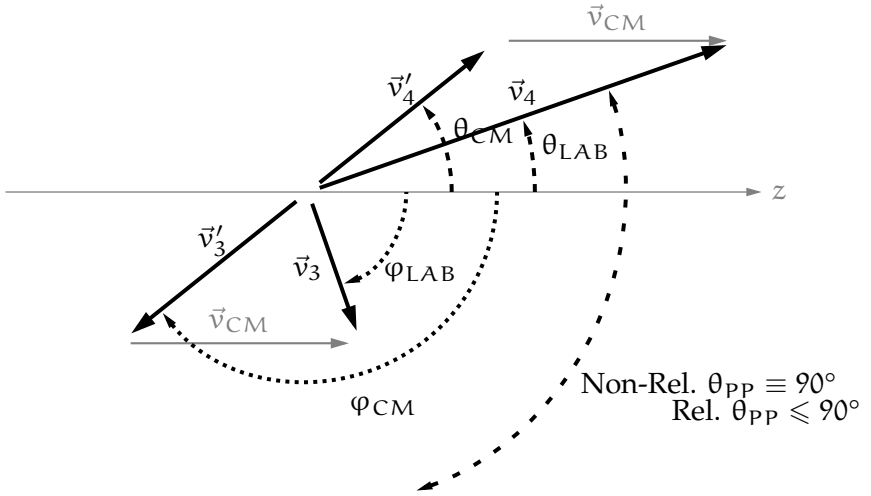

Figure 31: Reference system change for the specific case of the proton-proton elastic scattering. Velocity modules in the c.m. frame, v'_3 and v'_4, are equal to that of the centre of mass in the lab. frame, v_{CM}. In non-relativistic conditions the θ_{PP} angle is 90°, instead in relativistic condition it can be smaller.

from which it results

$$\begin{aligned}
\theta_{PP} = \varphi_{LAB} - \theta_{LAB} &= \arctan\left(\frac{\sin\varphi_{CM}}{1+\cos\varphi_{CM}}\right) - \arctan\left(\frac{\sin\theta_{CM}}{1+\cos\theta_{CM}}\right) \\
&= \arctan\left(\frac{\frac{\sin\varphi_{CM}}{1+\cos\varphi_{CM}} - \frac{\sin\theta_{CM}}{1+\cos\theta_{CM}}}{1+\frac{\sin\varphi_{CM}\sin\theta_{CM}}{1+\cos\theta_{CM}\cos\varphi_{CM}+\cos\theta_{CM}+\cos\varphi_{CM}}}\right) \\
&= \arctan\left(\frac{\frac{\sin\varphi_{CM}}{1+\cos\varphi_{CM}} - \frac{-\sin\varphi_{CM}}{1-\cos\varphi_{CM}}}{1+\frac{-\sin\varphi_{CM}\sin\varphi_{CM}}{1-\cos^2\varphi_{CM}}}\right) \\
\text{divergent argument} \quad &= \arctan\left(\frac{2\sin\varphi_{CM}}{1-\cos^2\varphi_{CM}-\sin^2\varphi_{CM}}\right) \longrightarrow \theta_{PP} \equiv 90°
\end{aligned}$$

Accordingly the relative angle between the two protons should be always 90°, in case of non-relativistic velocities. Actually during the proton runs the beam energy is $E_k = 177\,MeV$, hence, according with the relativistic formalism, the velocity in natural units is

$$\beta = \frac{P}{E} = \frac{\sqrt{E^2 - M^2}}{E} = \frac{\sqrt{(E_k + M)^2 - M^2}}{(E_k + M)} > 50\%,$$

which forces us to use a relativistic approach also for the emitted protons.

Relativistic approach

The centre-of-mass velocity in the laboratory frame is

$$\vec{v}_{CM} = \frac{\vec{p}_1 + \vec{p}_2}{E_1 + E_2} = \frac{\vec{p}_1}{E_{tot}},$$

where $\vec{p}_{1,2}$ and $E_{1,2}$ are the components of the particle four-vector. In natural units v_{CM} is about 0.294.

For the velocities, the Lorentz transformations used to pass from the c.m. to the laboratory frame in special relativity are:

$$\begin{aligned} v_x &= \frac{v'_x}{\gamma(1+v_{CM}v'_z)}\,, \\ v_y &= \frac{v'_y}{\gamma(1+v_{CM}v'_z)}\,, \\ v_z &= \frac{v'_z+v_{CM}}{1+v_{CM}v'_z}\,, \end{aligned} \tag{5.4}$$

where $\gamma = \dfrac{1}{\sqrt{1-v_{CM}^2}}$ is the Lorentz factor for the c.m. velocity in the laboratory frame.

Similarly to the relation (5.3), the angle transformation is determined by

$$\tan\theta_{LAB} = \frac{v_\perp}{v_z} = \frac{v'\sin\theta_{CM}}{\gamma\,(v_{CM}+v'\cos\theta_{CM})} = \frac{\sin\theta_{CM}}{\gamma\left(\frac{v_{CM}}{v'}+\cos\theta_{CM}\right)},$$

in which now we note the presence of the Lorentz factor.

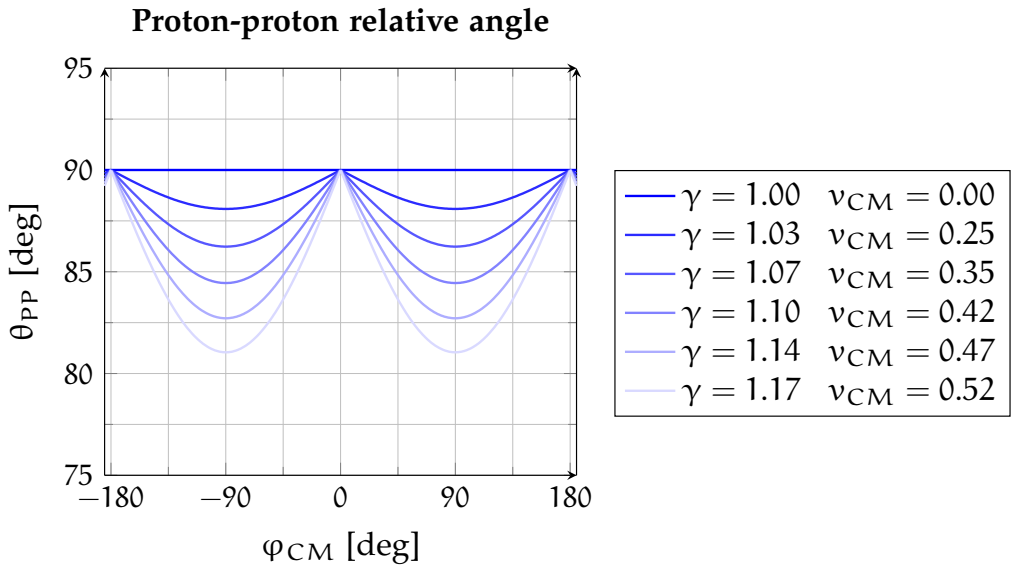

Figure 32: Correlation between the emission angle φ_{CM} (in c.m. frame) of one proton and the relative angle θ_{PP} (in lab. frame) with the other proton for several possible γ values.

Hence we calculate θ_{PP} in the same way as previously

$$\begin{aligned}\theta_{PP} =& \varphi_{LAB} - \theta_{LAB} \\ =& \arctan\left(\frac{\sin\varphi_{CM}}{\gamma\left(\frac{v_{CM}}{v'} + \cos\varphi_{CM}\right)}\right) - \arctan\left(\frac{\sin\theta_{CM}}{\gamma\left(\frac{v_{CM}}{v'} + \cos\theta_{CM}\right)}\right) \\ =& \arctan\left(\frac{\frac{\sin\varphi_{CM}}{\gamma\left(\frac{v_{CM}}{v'}+\cos\varphi_{CM}\right)} - \frac{\sin\theta_{CM}}{\gamma\left(\frac{v_{CM}}{v'}+\cos\theta_{CM}\right)}}{1 + \frac{\sin\varphi_{CM}\sin\theta_{CM}}{\gamma^2\left[\left(\frac{v_{CM}}{v'}\right)^2+\cos\theta_{CM}\cos\varphi_{CM}+\frac{v_{CM}}{v'}\cos\theta_{CM}+\frac{v_{CM}}{v'}\cos\varphi_{CM}\right]}}\right),\end{aligned}$$

with the same conditions $v_{CM}/v' = 1$ and $\cos\theta_{CM} = -\cos\varphi_{CM}$ it results

$$= \arctan\left(\frac{\frac{\sin\varphi_{CM}}{\gamma(1+\cos\varphi_{CM})} - \frac{-\sin\varphi_{CM}}{\gamma(1-\cos\varphi_{CM})}}{1 + \frac{-\sin\varphi_{CM}\sin\varphi_{CM}}{\gamma^2[1-\cos^2\varphi_{CM}]}}\right) = \arctan\left(\frac{2\gamma\sin\varphi_{CM}}{\gamma^2\left[1-\cos^2\varphi_{CM}\right] - \sin^2\varphi_{CM}}\right)$$

$$= \arctan\left(\frac{2\gamma\sin\varphi_{CM}}{(\gamma^2-1)\sin^2\varphi_{CM}}\right) = \arctan\left(\frac{2\gamma}{(\gamma^2-1)\sin\varphi_{CM}}\right) \longrightarrow \theta_{PP} \leqslant 90°$$

Contrary to the non-relativistic result, we obtain a non-constant value for each combination of emission angles. The non-relativistic behaviour is found for γ equals to 1. In Fig. 32 the dependence between one particle angle (in the c.m. frame) and the relative angle θ_{PP} (in the laboratory frame) is shown. Note that with the emission at $\varphi_{CM} = 90°$ the relative angle is minimized.

The minimum relative angle in our p-p scattering runs is $\theta_{PP}^{min} = 87.42°$, with $\gamma = 1.046$.

5.4.2 Experimental data

Ascertained the right expected value of θ_{PP}, we plotted the 2D-histogram of Fig. 33 in which the horizontal axis and the vertical axis represent the z-position of the reaction vertex (z_R) and the θ_{PP} values, respectively. The analysis result is in blue and here the tracks, which had the minimal distance D_{min} higher than 3 mm, were discarded since this could correspond to a bad reconstruction. The mean value of the relative angle is higher than 90°, contrary to kinematic expectations.

Moreover the distribution of θ_{PP} is not constant with the depth into the target of the reaction vertex, but it proportionally increases. The dependence can be partially explained with the energy decrease of the projectile into the LH2 target. Indeed the energy loss led the reaction energy at lower and lower values, cancelling the relativistic component. This fact, however, does not justify such an important dependence, and it could not cause the 90° threshold to be exceeded.

Regarding the proton polar angles used to obtain the relative angle θ_{PP}, we underline that, obviously, they coincide with the laboratory angles φ_{LAB} and

θ_{LAB} only if the projectile beam is perfectly collimated in the z-axis direction. Otherwise θ_{PP} has to be calculated not as the simple sum of the laboratory angles but using the complete information of the particle direction and remembering the inverse of the scalar product formula:

$$\theta_{PP} = \arccos \frac{\vec{v}_3 \cdot \vec{v}_4}{v_3 \cdot v_4}.$$

This observation is very important in case of heavier beam particles and the calculation of the fragment angular distribution.

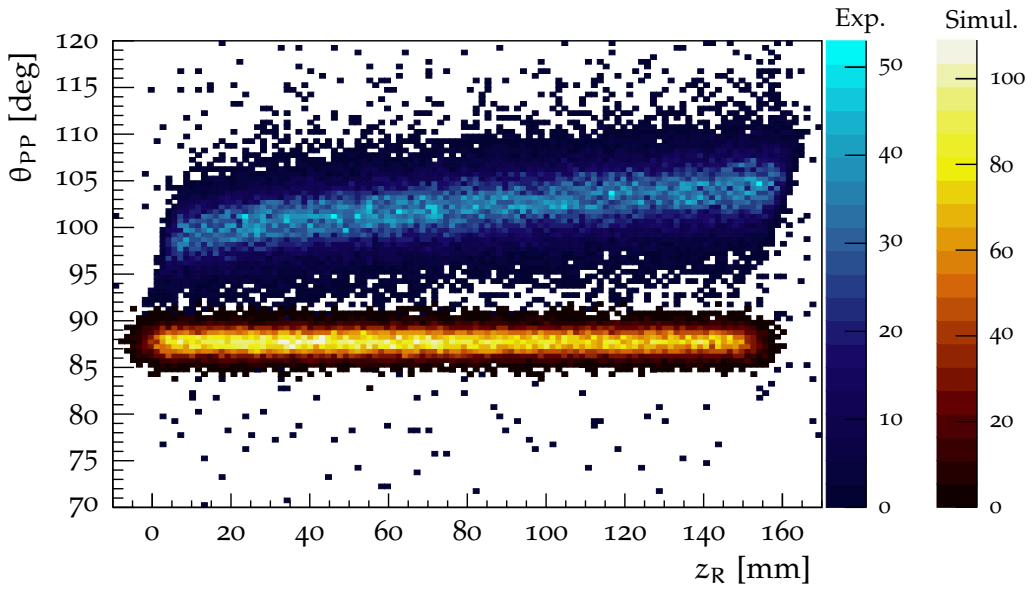

Figure 33: 2D-histogram of the relative angle of the emitted proton directions, θ_{PP}, respect to the reaction z-position z_R. In blue the result from the experiment analysis, in orange the simulation data of the two-body reaction calculation.

5.4.3 Simulation

In order to take into account the geometric contribution of the setup and the possible particle straggling due to the materials, we simulated a two-body reaction with the virtual arrays as explained in Sec. 3. It is important to underline that for the reaction simulation a *constant* differential cross section was used. The correct proton-proton differential cross section can be implemented in NPTool, although the available literature is scarce for energies like those of our experiment, $E_k^{proton} \simeq 177\,MeV$. Events in which not even a single proton was detected by DALI were discarded.

At the moment, the θ_{PP} and z_R values, used for the orange histogram in Fig. 33, are the kinematic data of the two-body reaction calculation. When the MINOS virtual array will be updated, the used data can be originated from the same track reconstruction of the experimental one. An artificial resolution has been inserted both for θ_{PP} and for z_R, respectively of 1° and 3 mm.

The 2D-histogram obtained by means of the simulation data confirmed that θ_{PP} should be lower than 90°. The increase of the θ_{PP} average value respect to the depth into the target is expected as described at the end of Sec. 5.4.2, but it cannot be appreciated because of the angular and spatial resolutions.

5.4.4 Test of the track linear fitting

A new method was necessary to explain and to study the discrepancy of the experiment results. The analysis codes were upgraded in order to allocate the number of the correspondent ring of pads from which the signal was detected. By convention, numbering was increasing from the innermost ring to the outer ring.

The good fitting of the (x, y, z) information to reconstruct the tracks was checked. In order to do that the minimal distances between the track and the points were calculated. These discrepancies were collected by ring number in the histograms in Fig. 34.

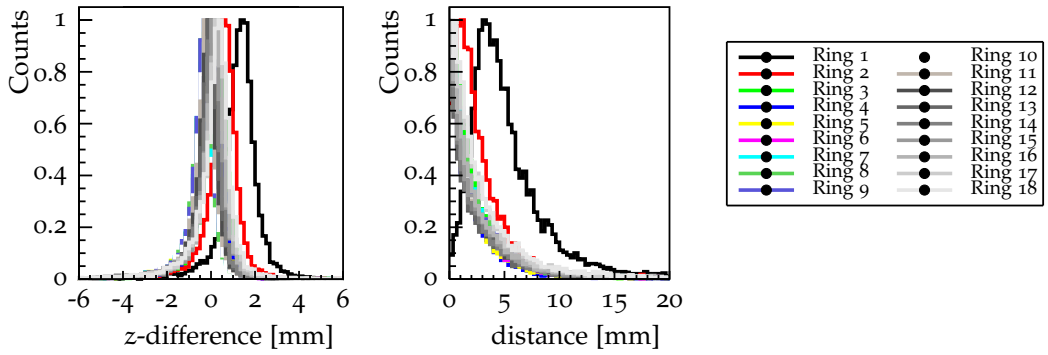

Figure 34: Track discrepancies in the S34 analysis. For each ring the discrepancies between the data points and the belonging track were calculated. The difference between the z-position of the ionization point and of the track are shown at left. At right the discrepancies are shown considering the distance between points and track. A strong discrepancy was noted for the first and the second rings. Counts were normalized with the number of each ring.

Fitted values highlight larger discrepancies for the inner rings, contrary to the outcomes of a previous experiment in which the collected data did not present this problem as can be seen in Fig. 35.

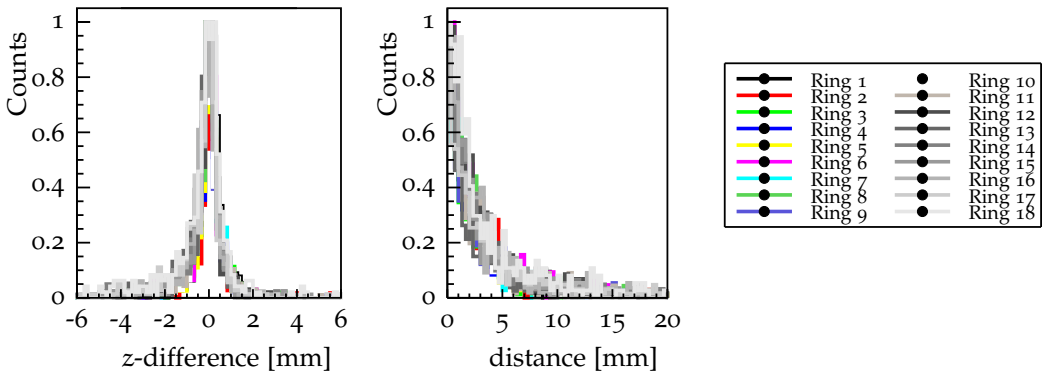

Figure 35: Track discrepancies in the analysis of a previous experiment, S18. As in Fig. 34 the discrepancies were calculated. On the contrary of S34 experiment, the discrepancy was minimized and homogeneous for each ring. Counts were normalized with the number of each ring.

In order to solve the problem, the analysis was repeated excluding the first two rings, however the discrepancies for the innermost rings remained and increased, and the strange θ_{PP} value persisted.

5.4.5 ByRing method

In order to identify the problem, the standard v_{drift} measurement, explained in Sec. 5.2, was then exploited for each pad ring and not for the entire pad plane. The graph in Fig. 36 presents a drastic change of the T_{Stop} value for the last rings.

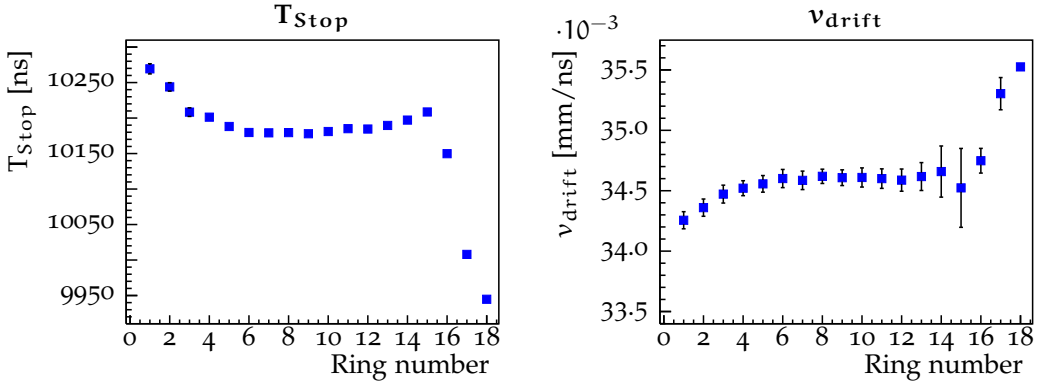

Figure 36: Analysis of the v_{drift} by ring for one acquisition run. At left the T_{Stop} values of which the errors are not visible. At right the v_{drift} values.

Because the non-constant v_{drift} values in the rings, it was supposed that the electric field changed with a radial gradient, despite the radial homogeneity with which MINOS has been designed.

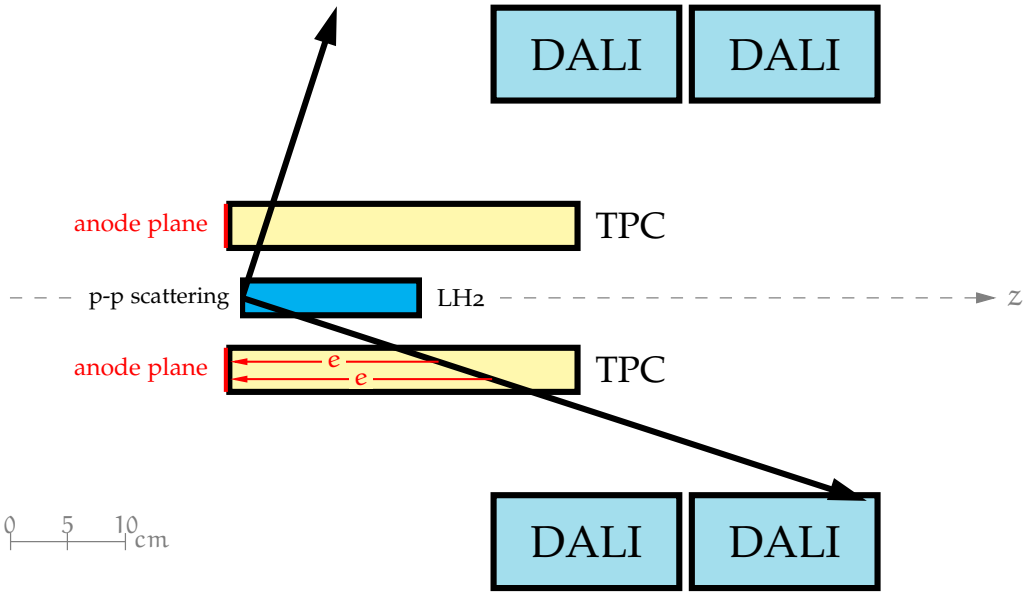

Figure 37: Scheme of the gas ionization and the electron collection. The DALI crystals were the acquisition trigger. Note that the z-position along the track is always increasing with the outer rings of the anode plane.

Actually, our geometry setup and the choice of DALI as trigger forced us to consider more accurately the track detection by the TPC. For example in the p-p scattering 90° was the maximum angle at which it was possible the proton was scattered. Moreover, as shown in Fig. 37, the particle ionized the gas in different z-positions in its passage. For each event the ionization z-position increased with the increasing position in the track.

Also taking into account the contribution of all the events, the positions of the gas ionizations in TPC were not equally distributed long the z-axis. For that it is not sure that we correctly estimated the beginning of TPC measuring the T_{Start} of time distribution.

Furthermore this inhomegeneity fell between the rings, since the obvious dependence between the position in the emission track and the distance from the z-axis.

In particular, because DALI was the trigger, the protons detected by the crystals could have reached the final TPC plane at most at the last ring levels. This explains the different T_{Start} and T_{Stop} position between the first and the last rings.

Simulation of the t_{pad} distributions by rings

The simulation I developed during this work allowed us to study in detail the effect of the assumption made in already existing approaches to this calibration.

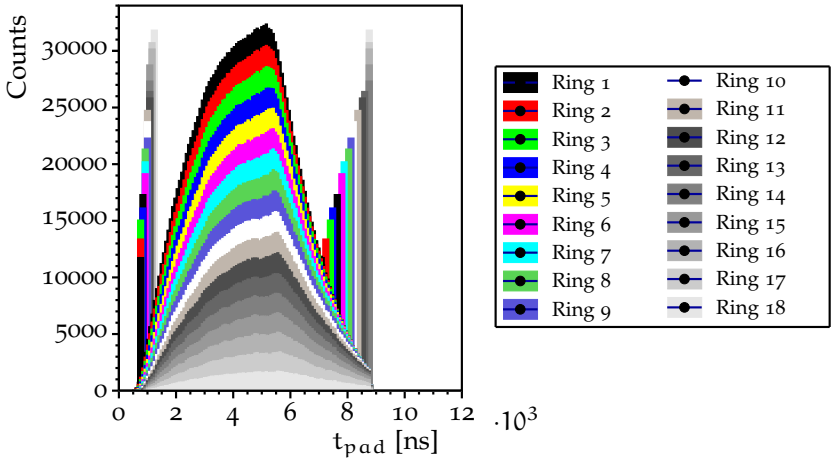

Figure 38: Simulation of the t_{pad} distributions by rings. Each coloured region represents the t_{pad} histogram of one ring. The vertical lines correspond to the T_{Start} and T_{Stop} positions.

Figure 38 shows the simulated t_{pad} distributions for each ring with an hypothetical common v_{drift}. In this histogram the time distributions were stacked one over the other and the vertical lines correspond to the T_{Start} and T_{Stop} positions. The total histogram corresponds to the entire t_{pad} distribution as in Fig. 26.

Note the difference about 2000 ns between the T_{Stop} of the first and of the last ring, while their T_{Start} values differ by 500 ns.

In this simulation the gap, between the T_{Start} position and the zero point, was not due to a detection delay. It resulted from the geometrical effects we are describing now and from the contribute of the displacement between the beginning of the TPC and the target, as we reported in Sec. 3.1.1.

Moreover the T_{Stop} value reached a maximum value with the last rings because the end of the TPC length. Hence we could establish that the T_{Stop} position of the entire time distribution corresponded to the effective end of the TPC.

Regarding the T_{Start} position, its measurement was experimentally made by the detection of a peak in the t_{pad} distribution as shown in Fig. 26. This peak was the end of the background noise and it is plausible to consider it as the beginnning of the TPC. If only because, otherwise, the considered length L_{TPC} in the Eq. (5.1) should be smaller, further decreasing the calculated v_{drift} (cfr. end of Sec. 5.2).

5.4.6 Reaction vertex distribution

In order to deal the issue in another perspective, the reaction vertex distributions were studied for the simulation and the experiment data. Figure 39 shows the two histograms corresponding to the projection in the x-axis of the 2D-histograms of Fig. 33.

We remember that, for the simulation data, the z_R positions 0 and 152.7 mm coincide to the beginning and the end of the target, respectively.

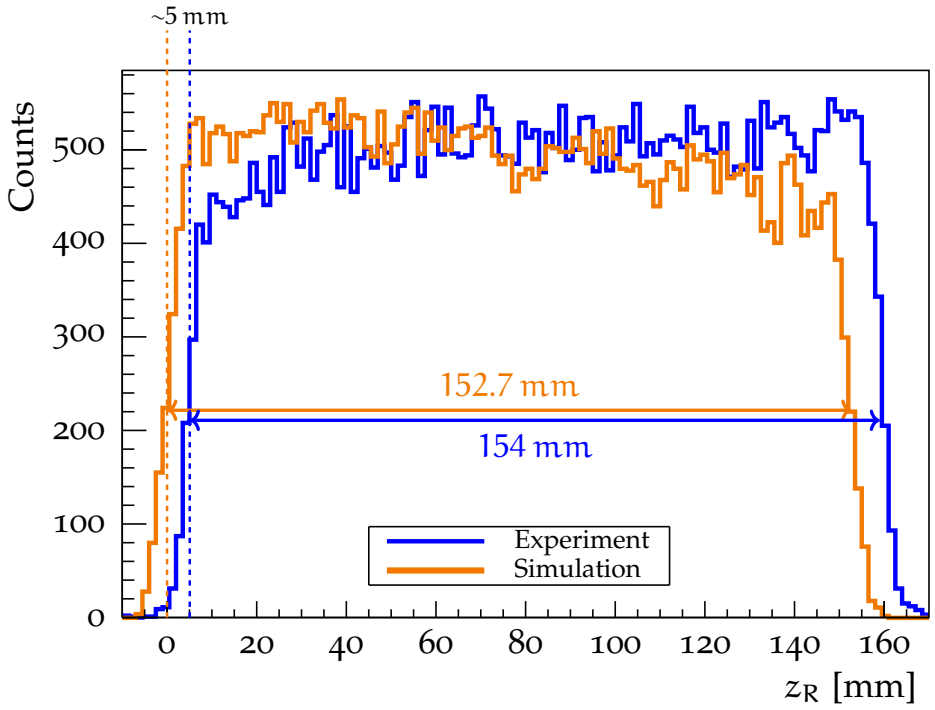

Figure 39: Distributions of the reaction vertices along the z direction. In blue the result from the experiment analysis, in orange the simulation data of the two-body reaction calculation.

To the contrary, for the experimental data those correspond to the position of the target extremes with respect to the TPC pad plane.

In this analysis the target was measured displaced from the pad plane by 5(1) mm and the length was 154(2) mm.

We therefore found measurements compatible with our experimental setup although the reconstruction of angles and particle directions seemed to be incorrect.

6 CONCLUSION AND OUTLOOK

The data analysis of the SAMURAI-34 experiment had begun with the purpose of studying the spectroscopy of the ^{7}H and of proving the tetraneutron existence. This will contribute significantly to the knowledge of nuclear interaction.

In this thesis the direct reaction ^{8}He(p, 2p)^{7}H was presented, its convenience and utilization (see Sec. 1.3). In particular, we focused on two detectors, MINOS and DALI, whose main duty is the identification of the reaction vertex and of the tracks of the emitted proton(s) (see Sec. 2.2-2.3). This information is fundamental for a correct energy reconstruction of the reaction products.

The geometrical setup of these two detectors was described and the simulations developed in my work, together with their analysis tools, were presented (see Sec. 3).

In Ch. 4 the light output linearity of the DALI NaI crystals was successfully proved and a first calibration was performed using cosmic muons. In order to achieve that, two coincidence requirements between the scintillators were adopted, highlighting the calibration peaks in the energy spectra. The energies of the obtained peaks were predicted first by a theoretical estimate and then by means of simulations. The obtained values were finally considered for the calibration. In this step we compared the experimental and simulated data, and we measured the crystal energy resolution $\Delta E = 1.36(4)\,MeV$.

Afterwards, in Ch. 5, the observables provided by the 3604 micro-detectors of MINOS were described, and their use for the track identification was explained. About the electron drift speed in the TPC, it was noticed that the mean value measured was around $0.0345(2)\,mm/ns$. The value was smaller than that expected and measured in previous experiments involving MINOS, the discrepancy was about $0.01\,mm/ns$, i.e. more than 20% lower. The presence of a large amount of impurities in the TPC chamber or other external factors could motivate this difference.

I improved the analysis codes for the proton track reconstruction and I began the calibration procedure of MINOS. In Sec. 5.4 the calibration using the p-p elastic scattering was motivated and described. Considering the projectile speed higher than $0.5\,c$, the relativistic approach was necessarily adopted and the relative angle θ_{pp} between the outgoing protons was calculated to range in values from 87.42° to 90°.

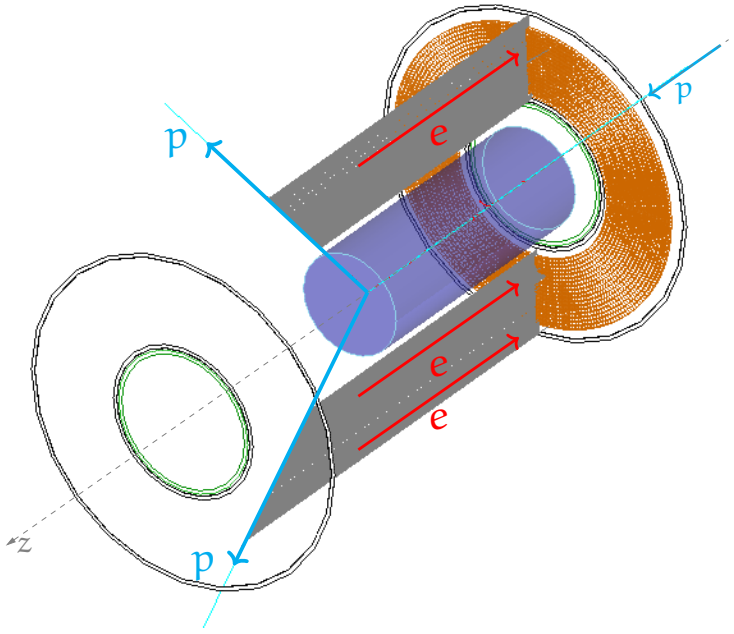

Figure 40: Simulation of a p-p scattering and the drift electrons originated by the gas ionization in MINOS. From right the proton marked with the small blue arrow reachs the target and the interaction occurs. The two outgoing protons are marked with the long blue arrows and the electrons are originated from the ionization. In red the electron direction towards the orange detector pad plane.

In contrast, the experimental result differed from the expectation: the measured θ_{pp} values exceeded 90° and they increased with the reaction vertex position along the target.

Simulating the p-p scattering, in order to take into account the geometry setup and the particle-matter interaction, the previous calculation was confirmed as shown in Fig. 33.

In Sec. 5.4.4 the good fitting procedure of the (x, y, z) information to reconstruct the tracks was checked and increasingly large discrepancies were highlighted for the inner rings of the detection pad plane. The fit could not be improved excluding some problematic rings.

After that, the MINOS detection was segmented by rings and studied in order to explain this behavior. The developed simulation supported a deeper knowledge of the device, especially with respect to the risks and the importance of choosing the proper trigger condition in the data acquisition.

Finally, changing perspective of physics, in Sec. 5.4.6 the reaction vertex distribution was studied for the simulated and the experimental data. From this comparison we estimated the displacement of the target by $5(1)$ mm with respect to the MINOS anode plane along the z-axis, and the target resulted $154(2)$ mm long. We therefore found measurements compatible with our experimental setup

although the reconstruction of angles and particle directions seemed to be incorrect.

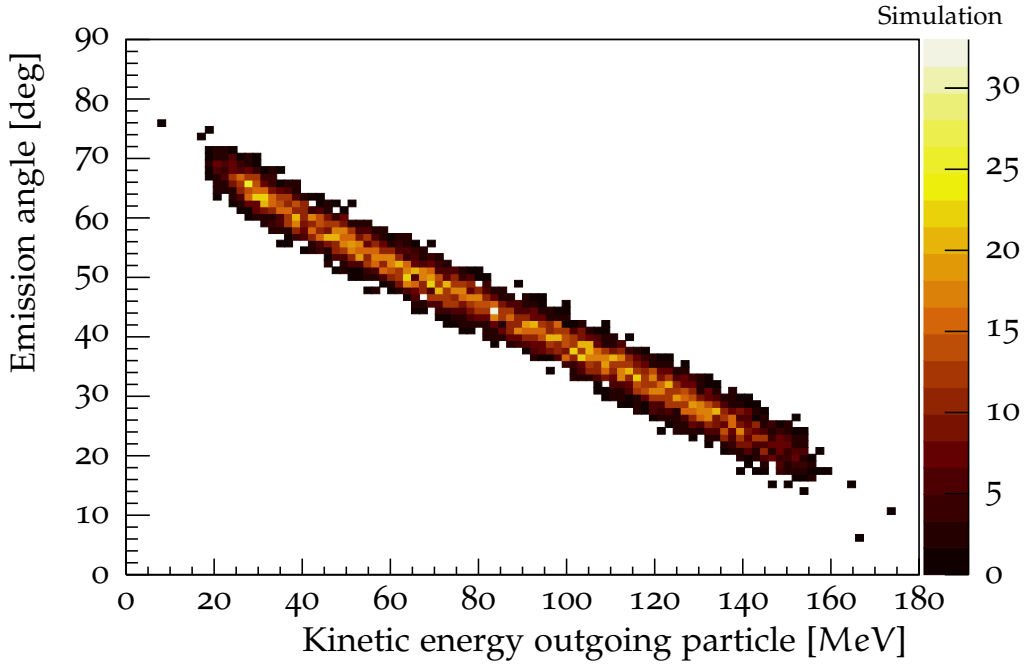

Figure 41: Correlation in simulation data between the polar angle of the proton direction and the kinetic energy of the same outgoing proton in the reaction vertex.

In order to overcome this problem, further studies are welcome and the improvement of the simulation can support them. In last months a partial improvement has been made in the virtual MINOS configuration. The possibility of simulating drift electrons, and their path up to the anode plane, has been added. Figure 40 shows the simulation of a p-p scattering in the MINOS target and the drift electrons originated by the gas ionization. This improvement, now begun by C. Lenain (LPC), has to be completed in order to use the same track reconstruction code cited in Sec. 5.3 for both experiment and simulation data. This will allow to measure the uncertainties due to the computational handling.

Moreover, it is also important to join in a better model of the differential cross-section for the proton-proton collision, as well as a hypothetical angular distribution for the ^{8}He(p, 2p)^{7}H reaction products to support the physical analysis of the experiment.

We can already illustrate some useful information that will be optimized by these developments. For example, the histogram with *emission angle VS vertex kinetic energy* of Fig. 41 shows the correlation of these two quantities (the emission angle of the particle and its kinetic energy in the reaction vertex) taking into account the relativistic contribution. Another less naive correlation is the *vertex kinetic energy VS detected energy* histogram (top panel in Fig. 42), from which it is

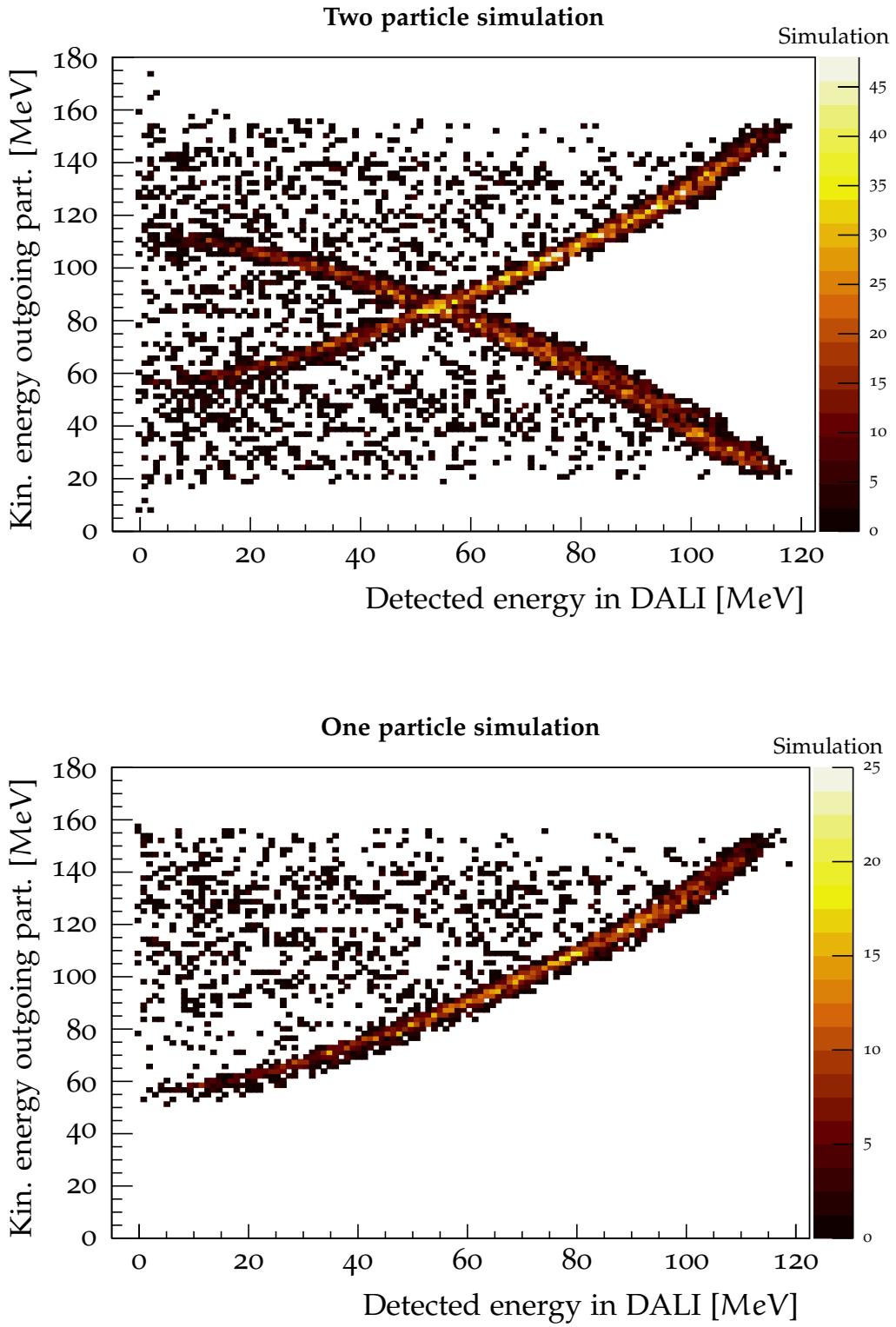

Figure 42: Correlation in simulation data between the kinetic energy of the outgoing proton in the reaction vertex and the detected energy in the DALI crystals. At top the result simulating the two-body scattering in which the characteristics of the outgoing particles are mixed; at bottom the simulation result using the two-body kinematics, but generating only one outgoing proton. The simulation at bottom is useful to have a forecast about the energy loss of the outgoing particles.

possible to know the proton energy loss in the material as the outgoing direction varies. Obviously, only one of the two marked lines corresponds to the proper correlation, i.e. that with an increasing slope. The decreasing line is relative to an information mixing: the detection of the energy of one particle but the kinetic energy of the other one. In fact, simulating the two-body reaction generating only one outgoing proton, as shown in the bottom panel of Fig. 42, only the increasing slope is present. From these histograms it is possible to estimate the energy loss, that should be from 40 to 60 MeV for the smallest and largest angles, respectively.

Regarding the continuation of the data analysis, the spatial resolution for the reaction vertex position will be improved by the BDC information (see Sec. 2.1.1).

The controversial issue remains and, at the moment, the S34 experiment could guarantee only a part of the desired goals. Partial physical results for the ^{8}He(p, 2p)^{7}H reaction should be obtained at the beginning of next year. The deficiency of the complete use of these two detectors, presented in this thesis, does not preclude the possibility of using the missing-mass method given in Sec. 1.3.1. This will offer the description of the ^{7}H, although the resolution cannot be excellent. The tetraneutron will be more unlikely measured.

7 APPENDIX

7.1 SIMULATION OUTPUT

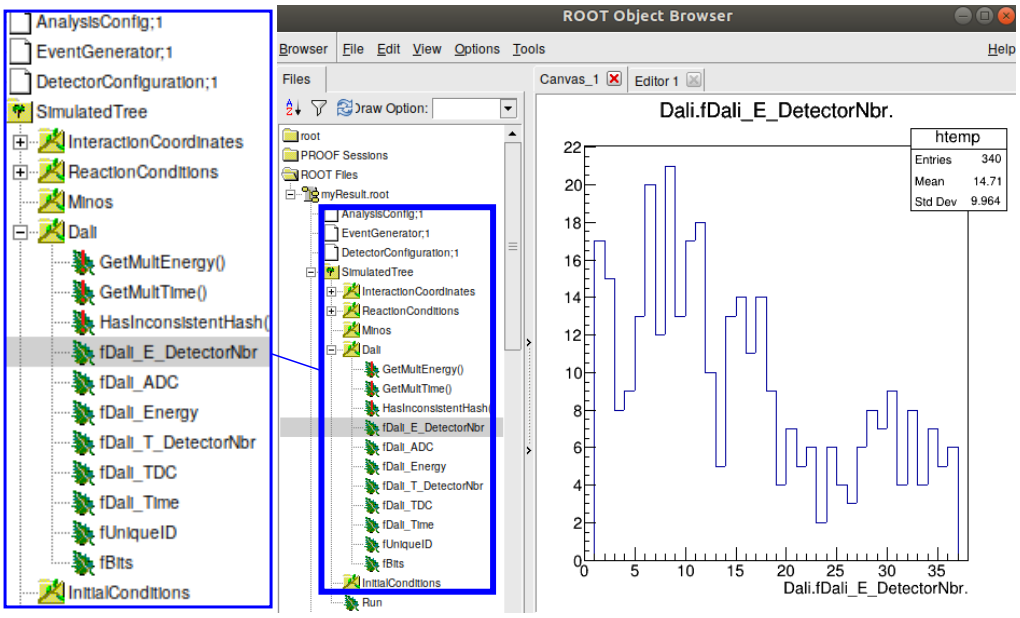

Figure 43: The browser window of ROOT reading the output file of a DALI simulation. On left-hand side the file manager shows the Dali structure that I designed to hold the experimental and simulated raw data; on right-hand side an example histogram shows the number of counts for each of the 36 DALI crystals.

The results of the simulation are in the ROOT format and the output file is stored in the $NPTOOL/Output/Simulation directory. A browser window of ROOT is shown in Fig. 43. On right-hand side, we display the distribution of the collected events sorted by the detector number. On left-hand side the file manager shows the nested objects in the file:

- AnalysisConfig: the text file with the configuration for a possible analysis;
- EventGenerator: the event generator text file used for the simulation;
- DetectorConfiguration: the detector geometry text file used for the simulation;

- SimulatedTree: the ROOT tree containing the results of the simulations.

The output ROOT tree contains three or more branches:

InteractionCoordinates. It mainly records the Cartesian and spherical coordinates of interaction between a particle and a detector.

ReactionConditions. It stores all kinematical information of the simulated reaction and its position.

***Detector*Data.** These classes store the results of the simulation concerning the detectors. Independently from the number and shape of the detectors involved in the geometry, only one branch is created for the whole kind of detector. For each event, the detector numbers are recorded as well as the energy and time for the units which were fired.

InitialConditions. It records all the information concerning the event generator, such as the vertex of interaction, the angles of emitted particles in the center of mass and laboratory frames, etc

7.2 RESPONSE SIGNAL OF A SCINTILLATOR

An important characteristic of these scintillators is their different light output depending on the nature of the detected particle, whether charged particle or gamma radiation.

With a ^{60}Co source and the NaI crystals, the 2 most likely interactions of its photons are the Compton or the Photoelectric interactions, corresponding respectively to the partial or total transfer of the γ-ray energy to an electron of the scintillator crystal.

In the scintillator, this photoelectron creates a large number of electron-hole pairs, and the de-excitation of the electrons generates the photon emission in the visible light spectrum. Then, these visible photons pass though the glass windows and are converted to an electrical signal when hitting the photocathode of the PMT.

A same kind of energy release occurs with more energetic heavy charged particles, but the different mean energy loss per distance, given by the Bethe formula

$$-\left\langle \frac{dE_{loss}}{dx} \right\rangle = \frac{4\pi}{m_e c^2} \cdot \frac{nz^2}{\beta^2} \cdot \left(\frac{e^2}{4\pi\epsilon_0} \right)^2 \cdot \left[\ln \frac{2m_e c^2 \beta^2}{I \cdot (1-\beta^2)} - \beta^2 \right],$$

is bigger, and it includes other effects such as saturation or quenching. The later represents all the loss mechanisms in the conversion of the particle energy to scintillation light. For instance, when an electron is captured at an activator site.

Certain radiationless transitions are possible between some excited states formed by electron capture and the ground state, in which case no visible photon results. Additional details can be found in [Kno10, p. 225].

BIBLIOGRAPHY

[Ago+03] S. Agostinelli et al. "GEANT4: A Simulation toolkit". In: *Nucl. Instrum. Meth.* A506 (2003), pp. 250–303. DOI: 10.1016/S0168-9002(03)01368-8.

[Ana+98] K Anami et al. "Light output response of GSO(Ce) and NaI(Tl) to protons up to 160 MeV". In: *Nuclear Instruments and Methods in Physics Research Section A-accelerators Spectrometers Detectors and Associated Equipment - NUCL INSTRUM METH PHYS RES A* 404 (Feb. 1998), pp. 327–333. DOI: 10.1016/S0168-9002(97)01160-1.

[Baz+02] D. Bazin et al. "The program LISE: a simulation of fragment separators". In: *Nuclear Instruments and Methods in Physics Research Section A: Accelerators, Spectrometers, Detectors and Associated Equipment* 482.1 (2002), pp. 307 –327. ISSN: 0168-9002. DOI: https://doi.org/10.1016/S0168-9002(01)01504-2. URL: http://www.sciencedirect.com/science/article/pii/S0168900201015042.

[Bee08] Beaumel and et al.ii. In: PISA Workshop, 2008.

[BR97] R. Brun and F. Rademakers. "ROOT: An object oriented data analysis framework". In: *Nucl. Instrum. Meth.* A389 (1997), pp. 81–86. DOI: 10.1016/S0168-9002(97)00048-X.

[BRR08] Walter Blum, Werner Riegler, and Luigi Rolandi. *Particle detection with drift chambers; 2nd ed.* Berlin: Springer, 2008. DOI: 10.1007/978-3-540-76684-1. URL: https://cds.cern.ch/record/1105920.

[BZ03] C A Bertulani and V Zelevinsky. "Is the tetraneutron a bound dineutron–dineutron molecule?" In: *Journal of Physics G: Nuclear and Particle Physics* 29.10 (Sept. 2003), pp. 2431–2437. DOI: 10.1088/0954-3899/29/10/309. URL: http://faculty.tamuc.edu/cbertulani/cab/papers/JPG_29_2003_2431.pdf.

[Cn+07] M. Caamaño et al. "Resonance State in ^{7}H". In: *Phys. Rev. Lett.* 99 (6 Aug. 2007), p. 062502. DOI: 10.1103/PhysRevLett.99.062502. URL: https://link.aps.org/doi/10.1103/PhysRevLett.99.062502.

[Cn+08] M. Caamaño et al. "Experimental study of resonance states in ^{7}H and ^{6}H". In: *Phys. Rev. C* 78 (4 Oct. 2008), p. 044001. DOI: 10.1103/PhysRevC.78.044001. URL: https://link.aps.org/doi/10.1103/PhysRevC.78.044001.

[For+06] S. Fortier et al. “Search for Resonances ^{4}n, ^{7}H and ^{9}He via Transfer Reactions”. English. In: Joint Institute for Nuclear Research, Dubna, Russia, 2006. URL: http://flerovlab.jinr.ru/linkc/eng_1/proceedings/exon06_cont.html.

[Gio+06] I. Giomataris et al. “Micromegas in a bulk”. In: *Nucl. Instrum. Meth.* A560 (2006), pp. 405–408. DOI: 10.1016/j.nima.2005.12.222. arXiv: physics/0501003 [physics].

[Gio+96] Y. Giomataris et al. “MICROMEGAS: a high-granularity position-sensitive gaseous detector for high particle-flux environments”. In: *Nuclear Instruments and Methods in Physics Research Section A: Accelerators, Spectrometers, Detectors and Associated Equipment* 376.1 (1996), pp. 29 –35. ISSN: 0168-9002. DOI: https://doi.org/10.1016/0168-9002(96)00175-1. URL: http://www.sciencedirect.com/science/article/pii/0168900296001751.

[HV62] Paul C. Hough V. “Method and means for recognizing complex patterns”. In: 3069654 (Dec. 1962). URL: http://www.freepatentsonline.com/3069654.html.

[Kno10] Glenn F Knoll. *Radiation detection and measurement; 4th ed.* New York, NY: Wiley, 2010. URL: https://cds.cern.ch/record/1300754.

[Kob+00a] T. Kobayashi et al. “ ” In: *Annual Report of HIMAC* (2000).

[Kob+00b] T. Kobayashi et al. “Nuclear Structure Studies using Proton/ Cluster-Knockout Reactions”. In: *HIMAC Report H12* (2000), p. 2. URL: http://lambda.phys.tohoku.ac.jp/~kobayash/HIMAC/files/HIMAC_Rep_H13.pdf.

[Kob+13] T. Kobayashi et al. “SAMURAI spectrometer for RI beam experiments”. In: *Nuclear Instruments and Methods in Physics Research Section B: Beam Interactions with Materials and Atoms* 317 (2013). XVIth International Conference on ElectroMagnetic Isotope Separators and Techniques Related to their Applications, December 2–7, 2012 at Matsue, Japan, pp. 294 –304. ISSN: 0168-583X. DOI: https://doi.org/10.1016/j.nimb.2013.05.089. URL: http://www.sciencedirect.com/science/article/pii/S0168583X13007118.

[Kor+] A. A. Korsheninnikov et al. “Studies of transfer reactions with exotic beams: superheavy hydrogen ^{5}H”. In: *Exotic Nuclei*, pp. 317–333. DOI: 10.1142/9789812777300_0025. eprint: https://www.worldscientific.com/doi/pdf/10.1142/9789812777300_0025. URL: https://www.worldscientific.com/doi/abs/10.1142/9789812777300_0025.

[Kor+03] A. A. Korsheninnikov et al. "Experimental Evidence for the Existence of ^{7}H and for a Specific Structure of ^{8}He". In: *Phys. Rev. Lett.* 90 (8 Feb. 2003), p. 082501. DOI: 10.1103/PhysRevLett.90.082501. URL: https://link.aps.org/doi/10.1103/PhysRevLett.90.082501.

[Kub03] Toshiyuki Kubo. "In-flight RI beam separator BigRIPS at RIKEN and elsewhere in Japan". In: *Nuclear Instruments and Methods in Physics Research Section B: Beam Interactions with Materials and Atoms* 204 (2003). 14th International Conference on Electromagnetic Isotope Separators and Techniques Related to their Applications, pp. 97 –113. ISSN: 0168-583X. DOI: https://doi.org/10.1016/S0168-583X(02)01896-7. URL: http://www.sciencedirect.com/science/article/pii/S0168583X02018967.

[LC05] Rimantas Lazauskas and Jaume Carbonell. "Three-neutron resonance trajectories for realistic interaction models". In: *Phys. Rev. C* 71 (4 Apr. 2005), p. 044004. DOI: 10.1103/PhysRevC.71.044004. URL: https://link.aps.org/doi/10.1103/PhysRevC.71.044004,https://arxiv.org/abs/nucl-th/0502037.

[Mat+16] A Matta et al. "NPTool: a simulation and analysis framework for low-energy nuclear physics experiments". In: *Journal of Physics G: Nuclear and Particle Physics* 43.4 (2016), p. 045113. URL: http://stacks.iop.org/0954-3899/43/i=4/a=045113.

[MM03] F.M. Marqués Moreno. "Haloes, molecules and multi-neutrons". In: *Lab. de Physique Corpusculaire* (2003), p. 32. URL: http://inis.iaea.org/search/search.aspx?orig_q=RN:34056282.

[Nik+10] E. Yu. Nikolskii et al. "Search for ^{7}H in ^{2}H + ^{8} He collisions". In: *Phys. Rev. C* 81 (6 June 2010), p. 064606. DOI: 10.1103/PhysRevC.81.064606. URL: https://link.aps.org/doi/10.1103/PhysRevC.81.064606.

[Obe+14] A. Obertelli et al. "MINOS: A vertex tracker coupled to a thick liquid-hydrogen target for in-beam spectroscopy of exotic nuclei". In: *Eur. Phys. J. A* 50.1 (2014), p. 8. DOI: 10.1140/epja/i2014-14008-y. URL: https://doi.org/10.1140/epja/i2014-14008-y.

[Pie03] Steven C. Pieper. "Can Modern Nuclear Hamiltonians Tolerate a Bound Tetraneutron?" In: *Phys. Rev. Lett.* 90 (25 June 2003), p. 252501. DOI: 10.1103/PhysRevLett.90.252501. URL: https://arxiv.org/pdf/nucl-th/0302048.pdf,https://link.aps.org/doi/10.1103/PhysRevLett.90.252501.

[RIK06] Group RIKEN. *Detector-BDC.pdf*. Tech. rep. RIKEN Nishina Center, 2006. URL: http://www.nishina.riken.jp/RIBF/SAMURAI/image/Detector-BDC.pdf.

[RIK08] Group RIKEN. *Detector-HOD.pdf*. Tech. rep. RIKEN Nishina Center, 2008. URL: ribf.riken.jp/SAMURAI/index.php?plugin=attach&refer=ChargedParticleDetector&openfile=Detector-HOD.pdf.

[San15] Clémentine Santamaria. "Quest for new nuclear magic numbers with MINOS". Theses. Université Paris Sud - Paris XI, Sept. 2015. URL: https://tel.archives-ouvertes.fr/tel-01231191.

[Sat+13] Hiromi Sato et al. "Superconducting dipole magnet for SAMURAI spectrometer". In: *Applied Superconductivity, IEEE Transactions on* 23 (June 2013), pp. 4500308–4500308. DOI: 10.1109/TASC.2012.2237225.

[SV63] J.P. Schiffer and R. Vandenbosch. "Search for a particle-stable tetra neutron". In: *Physics Letters* 5.4 (1963), pp. 292 –293. ISSN: 0031-9163. DOI: https://doi.org/10.1016/S0375-9601(63)96134-6. URL: http://www.sciencedirect.com/science/article/pii/S0375960163961346.

[Tak+14] S. Takeuchi et al. "DALI2: A NaI(Tl) detector array for measurements of γ rays from fast nuclei". In: *Nuclear Instruments and Methods in Physics Research Section A: Accelerators, Spectrometers, Detectors and Associated Equipment* 763 (2014), pp. 596 –603. ISSN: 0168-9002. DOI: https://doi.org/10.1016/j.nima.2014.06.087. URL: http://www.sciencedirect.com/science/article/pii/S0168900214008419.

[Tim03] N K Timofeyuk. "Do multineutrons exist?" In: *Journal of Physics G: Nuclear and Particle Physics* 29.2 (Jan. 2003), pp. L9–L14. DOI: 10.1088/0954-3899/29/2/102. URL: https://doi.org/10.1088%2F0954-3899%2F29%2F2%2F102.

[WL85] R. Voss W. Lohmann R. Kopp. "ENERGY LOSS OF MUONS IN THE ENERGY RANGE 1 GeV to 10 000 GeV". In: *CERN—Service d'Information scientifique* (Mar. 1985), pp. 29–33. URL: https://inis.iaea.org/collection/NCLCollectionStore/_Public/16/048/16048635.pdf.

[ZZB10] J. F. Ziegler, M. D. Ziegler, and J. P. Biersack. "SRIM - The stopping and range of ions in matter (2010)". In: *Nuclear Instruments and Methods in Physics Research B* 268 (June 2010), pp. 1818–1823. DOI: 10.1016/j.nimb.2010.02.091.